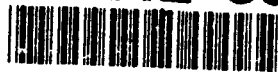


AD-A242 399



DTIC

ELECTE

NOV 5 1991

C



VELOCITY MEASUREMENTS IN HIGH TEMPERATURE GASES  
USING LASER-INDUCED NO FLUORESCENCE

M. G. Allen  
S. J. Davis

Physical Sciences Inc.  
20 New England Business Center  
Andover, MA 01810

October 1991

Final Report for period Aug 90 - Apr 91

Approved for public release; distribution is unlimited.

91-15004



AERO PROPULSION & POWER DIRECTORATE  
WRIGHT LABORATORY  
AIR FORCE SYSTEMS COMMAND  
WRIGHT-PATTERSON AIR FORCE BASE, OHIO 45433-6563

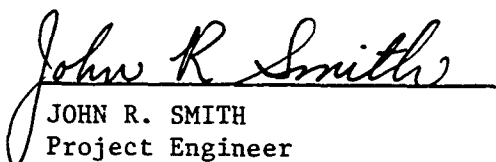
91 1104 075

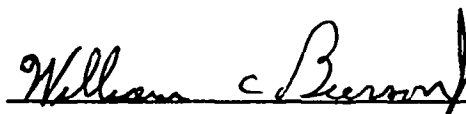
## NOTICE

When Government drawings, specifications, or other data are used for any purpose other than in connection with a definitely Government-related procurement, the United States Government incurs no responsibility or any obligation whatsoever. The fact that the government may have formulated or in any way supplied the said drawings, specifications, or other data, is not to be regarded by implication, or otherwise in any manner construed, as licensing the holder, or any other person or corporation; or as conveying any rights or permission to manufacture, use, or sell any patented invention that may in any way be related thereto.

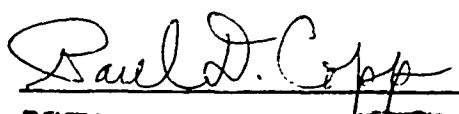
This report is releasable to the National Technical Information Service (NTIS). At NTIS, it will be available to the general public, including foreign nations.

This technical report has been reviewed and is approved for publication.

  
JOHN R. SMITH  
Project Engineer  
Propulsion Development Branch

  
WILLIAM C. BURSON JR, Chief  
Propulsion Development Branch  
Advanced Propulsion Division

FOR THE COMMANDER

  
PAUL D. COPP, LTCOL, USAF  
Deputy Director  
Advanced Propulsion Division  
Aero Propulsion & Power Directorate

If your address has changed, if you wish to be removed from our mailing list, or if the addressee is no longer employed by your organization please notify WL/POPR, WPAFB, OH 45433-6563 to help us maintain a current mailing list.

Copies of this report should not be returned unless return is required by security considerations, contractual obligations, or notice on a specific document.

UNCLASSIFIED

SECURITY CLASSIFICATION OF THIS PAGE

## REPORT DOCUMENTATION PAGE

1a. REPORT SECURITY CLASSIFICATION Unclassified			1b. RESTRICTIVE MARKINGS N/A		
2a. SECURITY CLASSIFICATION AUTHORITY N/A since unclassified			3. DISTRIBUTION/AVAILABILITY OF REPORT Approved for public release; distribution unlimited.		
2b. DECLASSIFICATION/DOWNGRADING SCHEDULE N/A since unclassified					
4. PERFORMING ORGANIZATION REPORT NUMBER(S) PSI-2145/TR-1108			5. MONITORING ORGANIZATION REPORT NUMBER(S) WL-TR-91-2109		
6a. NAME OF PERFORMING ORGANIZATION Physical Sciences Inc.		6b. OFFICE SYMBOL (if applicable)		7a. NAME OF MONITORING ORGANIZATION Aero Propulsion & Power Dir. (WL/POPR) Wright Laboratory	
6c. ADDRESS (City, State, and ZIP Code) 20 New England Business Center Andover, MA 01810			7b. ADDRESS (City, State, and ZIP Code) Wright-Patterson AFB, OH 45433-6563		
8a. NAME OF FUNDING/SPONSORING ORGANIZATION Wright Laboratory		8b. OFFICE SYMBOL (if applicable) WL/POPR		9. PROCUREMENT INSTRUMENT IDENTIFICATION NUMBER F33615-90-C-2069	
8c. ADDRESS (City, State, and ZIP Code) Aero Propulsion and Power Laboratory Wright-Patterson AFB, OH 45433-6563			10. SOURCE OF FUNDING NUMBERS		
			PROGRAM ELEMENT NO. 65502F	PROJECT NO. 3005	TASK NO. 21
11. TITLE (Include Security Classification) Velocity Measurements in High Temperature Gases Using Laser-Induced NO Fluorescence					
12. PERSONAL AUTHOR(S) M.G. Allen and S.J. Davis					
13a. TYPE OF REPORT Final		13b. TIME COVERED FROM Aug 90 TO Apr 91		14. DATE OF REPORT (Year, Month, Day) October 1991	
15. PAGE COUNT 66					
16. SUPPLEMENTARY NOTATION This is a Small Business Innovative Research Program, Phase I report.					
17. COSATI CODES			18. SUBJECT TERMS (Continue on reverse if necessary and identify by block number)		
FIELD	GROUP	SUB-GROUP			
19. ABSTRACT (Continue on reverse if necessary and identify by block number)					
<p>This report describes the results of a Phase I SBIR program which investigated the applicability of a Laser-Induced Fluorescence (LIF) velocimetry diagnostic technique based on Doppler-shifted NO fluorescence. The intent of the program was to quantitatively understand the potential accuracy of the approach in high-temperature, high-pressure gas flow applications when one is restricted to use only a single laser wavelength. The single laser wavelength approach greatly simplifies the experimental requirements while retaining the capability of simultaneous, multiple-point velocity field measurements. The report summarizes detailed analytical studies which demonstrate that, for representative NO lineshapes and available pulse-dye lasers, single-shot measurements of the instantaneous velocity field are possible in essentially uncharacterized pressure and temperature fields with</p>					
20. DISTRIBUTION/AVAILABILITY OF ABSTRACT <input checked="" type="checkbox"/> UNCLASSIFIED/UNLIMITED <input type="checkbox"/> SAME AS RPT. <input type="checkbox"/> DTIC USERS			21. ABSTRACT SECURITY CLASSIFICATION Unclassified		
22a. NAME OF RESPONSIBLE INDIVIDUAL John R. Smith			22b. TELEPHONE (Include Area Code) (513) 255-2175		22c. OFFICE SYMBOL WL/POPR

DD FORM 1473, 84 MAR

83 APR edition may be used until exhausted.  
All other editions are obsolete.

UNCLASSIFIED

SECURITY CLASSIFICATION OF THIS PAGE

## 19. Abstract (Continued)

→ less than 10 percent uncertainty. When *a priori* information on the pressure or temperature field is available, the instantaneous measurement uncertainty is reduced to less than 5 percent. The analytical conclusions are based on modeling of actual planar laser-induced fluorescence (PLIF) experimental configurations, commercially available laser parameters, and realistic signal uncertainty analyses. Several experimental tasks were also performed. Ultra-high resolution measurements of isolated NO fluorescence and absorption lineshapes were performed in order to extract their pressure and thermal broadening characteristics. Development also began on a high-temperature, high-pressure NO-laden gas flow which will be used as the validation test-bed in the Phase II program. The flow is derived from a high-pressure hydrogen-air burner whose exhaust products are accelerated to create a near atmospheric pressure, supersonic, underexpanded round jet. The results from the Phase I program clearly demonstrate the feasibility of the velocity field imaging instrument and have guided the prototype instrument design to be explored in the Phase II program.

# TABLE OF CONTENTS



## Section

## Page

	EXECUTIVE SUMMARY	vii
1.	INTRODUCTION	1
2.	BACKGROUND	4
2.1	Laser-Induced NO Fluorescence	4
2.2	Doppler-Shifted Fluorescence	8
2.3	Lineshape Broadening Mechanisms	10
3.	HIGH-RESOLUTION MEASUREMENTS OF NO LINESHAPE PARAMETER	13
4.	ANALYTICAL STUDY VELOCITY ALGORITHMS	20
4.1	Derivation of Velocity Algorithms	20
4.2	Pulsed Laser Excitation Scans	27
4.3	Velocity Algorithm Sensitivity Analysis	32
4.3.1	Variations Due to Temperature, Pressure, and Laser Bandwidth	33
4.3.2	Signal Noise Consideration	40
5.	DEVELOPMENT OF HIGH PRESSURE, SUPERSONIC BURNER	45
5.1	Burner Overview	45
5.2	PLIF Imaging of NO Distributions in Exhaust Jet	50

Accession For	
NTIS GRA&I	<input checked="" type="checkbox"/>
DTIC TAB	<input type="checkbox"/>
Unannounced	<input type="checkbox"/>
Justification	
By	
Distribution/	
Availability Codes	
Dist	Avail and/or Special
A-1	

## TABLE OF CONTENTS (Cont.)

<u>Section</u>	<u>Page</u>
6. CONCLUSIONS AND SUMMARY	53
7. ACKNOWLEDGEMENTS	55
8. REFERENCES	56

## LIST OF FIGURES

<u>Figure</u>		<u>Page</u>
1.	Schematic Energy Level Diagram Showing Important Processes in Laser-Induced NO Fluorescence	4
2.	Rotational Branches of NO A-X Transitions	6
3.	Schematic Illustration of the Geometry of the Linear Doppler-Shift	8
4.	Schematic of High-Resolution NO Lineshape Measurements	14
5.	Absorption and Fluorescence Data Traces from High Resolution Static Cell Measurements	16
6.	NO Absorption Lineshape Measurement	17
7.	An NO Voigt Lineshape for the $Q_1(33)$ Transitions and Its Derivatives	18
8.	Schematic Diagram of Optical Access for One-Dimensional Flow Measurements	21
9.	Molecular Absorption Lineshape and Laser Spectral Bandwidth Overlap for a Narrow-Bandwidth Laser	22
10.	Molecular Absorption Lineshape and Laser Spectral Bandwidth for a Broad-Bandwidth Laser	24
11.	Molecular Absorption Lineshape and Laser Spectral Bandwidth Overlap for Equivalent Bandwidths	26
12.	Experimental Setup for Pulsed Laser Excitation Scans	28
13.	Room Temperature NO Pulsed Laser Excitation Scan	29
14.	NO Excitation Scan Detail - 300 K	30
15.	NO Excitation Scan Detail - 1500 K	31
16.	Conceptual Outline of the Effect of Pressure on the Velocity Doppler-Shifted Overlap of the Laser Lineshape and Absorption Lineshape	34

## LIST OF FIGURES (Concluded)

<u>Figure</u>		<u>Page</u>
17.	Velocity Algorithm for Various Pressures	34
18.	Velocity Algorithm for Various Temperatures	36
19.	Velocity Algorithm for Isentropic Flow Variations	37
20.	Velocity Algorithm for Fluctuating Laser Bandwidth	39
21.	Velocity Algorithm for Shot-Noise Limited Signals	42
22.	Velocity Algorithm for Isentropic Flow Variations in the Presence of Signal Shot-Noise	43
23.	Schematic of High-Pressure Hydrogen-Air Burner	46
24.	Schematic Diagram of Underexpanded Jet Flowfield for an Expansion Ratio $\sim 7$	48
25.	Schematic Diagram of Underexpanded Jet Flowfield for an Expansion Ratio $\sim 3$	49
26.	NO PLIF Image in Supersonic Flowfield	51



## EXECUTIVE SUMMARY

The velocity measurement technique investigated in this program relies on the Doppler-shift of a molecular absorption line of a naturally occurring gaseous species in a high temperature flowfield. The magnitude of the shift is recorded as a normalized fluorescence signal, permitting measurements to be made remotely in the flowfield with high spatial resolution. We focus on the use of pulsed laser systems for the fluorescence excitation, further providing extreme temporal resolution.

- In the course of this program, the ground work was laid for the development and demonstration of Planar Laser-Induced Fluorescence (PLIF) velocimeter which would measure a single component of velocity in a plane within a high-temperature flow using a naturally occurring trace species - NO. This report describes the theory of Doppler-shifted LIF and details the sensitivity of the velocity measurement concept to fluctuations in flow pressure and temperature. Modeling of candidate experimental configurations is presented which predicts instrument accuracy taking into account the above fluctuations and realistic signal noise levels.
- Considerable effort was devoted toward the design, development, and shake-down of a high-pressure, high-temperature supersonic burner. This facility is capable of generating a wide range of flow conditions, nominally in the vicinity of Mach 3, 1500 K, and 1 atm and will constitute the primary test bed for Phase II development efforts. Preliminary characterization experiments were undertaken in both combusting and non-combusting modes. PLIF images of NO distributions in the exhaust flow were used to verify cold flow operation.
- Experiments were also conducted to make measurements of the detailed NO lineshape in order to determine pressure and thermal broadening parameters which are critical for calculation of flow velocity from fluorescence signals. A frequency-doubled, narrow-bandwidth (single mode) CW ring-dye laser was scanned over transitions of the NO A-X system in a static cell over a range of background gas pressures. The experimental absorption (and fluorescence) lineshapes were fit with calculated Voigt profiles to establish the pressure-dependent collisional broadening parameter.

A major result of this comprehensive Phase I program was the development of a detailed model that will guide in the design of the diagnostic instrument that will be constructed and tested in Phase II.

## 1. INTRODUCTION

The resurgence of interest in supersonic propulsion systems (SCRAMjets) and controlled hypersonic flight places new demands on experimental techniques for high temperature flow property measurements. Among the key parameters in vehicle performance assessment during design and development is the vector velocity field around the body and throughout the propulsion system. Current velocity measurement techniques, such as hot-wire anemometry and laser-Doppler anemometry are generally inapplicable in high-temperature, high-pressure, supersonic flow test facilities or are subject to large systematic errors. The NO fluorescence approach investigated in this Phase I SBIR program circumvents many of the inherent limitations in conventional velocity measurement technology and is eminently suited to measurements within SCRAMjet propulsion systems. Furthermore, the fluorescence approach will be capable of simultaneous, multi-point measurements using laser sheet illumination and fluorescence detection via sensitive, imaging detector arrays.

The experimental challenges associated with obtaining velocity measurements in high temperature, compressible flowfields are profound. Laser-Doppler Anemometry (LDA) techniques have been developed to the point where the three components of the mean and fluctuating velocity vector at a point in the flowfield can be measured. A single velocity component is measured by interfering two coherent beams (derived from a common laser source) at a point in the flowfield and detecting the period of the scattering signature from a particle traversing the resulting fringe pattern.

Although LDA finds common application in near-isothermal, low Mach number flows, it is not appropriate for all flows. In reacting flows, the density variations associated with the temperature variations in the flowfield bias the velocity statistics toward the cold portions of the flow (where the density of scattering centers is higher) and is known to skew the measured distribution of rms fluctuations. Furthermore, at the highest temperatures associated with air-breathing combustion systems (2000 to 3000 K), the seed particles

themselves (typically  $\text{Al}_2\text{O}_3$  or  $\text{TiO}_2$ ) breakdown so that no LDA signal is generated. Finally, in supersonic flows with shock waves, the relatively large ( $\sim 1 \mu\text{m}$ ) seed particles may not always track the velocity of the gas due to the particle inertia.

Hot-wire anemometry has been used in fluid dynamics research for decades. As an intrusive technique, it is inherently highly perturbing to the flowfield downstream of the probe. In supersonic flows, the perturbation may manifest itself as shock waves emanating from the probe or the probe support. Furthermore, the wire (or film) cannot survive the high temperatures associated with combustion. Hence, this technique is unsuitable for high temperature reacting flowfields. In addition, the wire responds to a combination of density, velocity, and temperature so that independent determination of any individual quantity is ambiguous.

Non-intrusive, laser-based gas velocity measurement approaches based on flow tagging have been suggested by several groups. Optical flow tagging approaches are based on marking a line or a cross in the flow with one laser beam and then probing the marked line with a second laser beam or sheet at a known time later. The displacement of the marked gas during the known time delay gives the average convection speed during the time between the two laser pulses. This basic approach has been demonstrated using seeded biacetyl,<sup>1</sup> nascent molecular oxygen (RELIEF method),<sup>2</sup> and water vapor.<sup>3,4</sup> Only the water vapor technique has promise for high temperature flows. The biacetyl seed is not stable above room temperature in the presence of oxygen. The marking of the gas in the RELIEF technique is accomplished via Raman excitation of an excited vibrational level in the oxygen ground electronic state and this level does not persist long enough at high temperatures to make a measurement.

The water vapor tagging approach uses a tunable KrF excimer laser to dissociate  $\text{H}_2\text{O}$  into, among other products, ground state OH in a thin line along the laser beam. At some later time, a second laser is used to excite this OH line in order to record its

displacement. No demonstrations to date have succeeded in reacting flows where the background nascent OH distribution overwhelms the visibility of the laser-tagged molecules.

It should be recognized that the flow tagging measurements are not a direct, spatially resolved measurement of the gas velocity. Indeed, the measurement yields meaningful results only in one-dimensional, or nominally one-dimensional, flows where no directional ambiguity of the marked gas is present. In multi-dimensional or strongly turbulent flows, the marked line or cross in the flowfield will be rapidly disrupted, rendering interpretation of the displaced fluid meaningless.

The approach investigated in our Phase I program is a *direct measurement of the velocity field* at every spatially-resolved detection point with no restrictions on the dimensionality or turbulence level of the flow. Furthermore, the flow tagging approaches require multiple wavelengths with concomitant expensive and complex laser systems, whereas the technique developed in this program is purposely designed to use a single, conventional pulsed-dye laser system.

## 2. BACKGROUND

### 2.1 Laser-Induced NO Fluorescence

The approach for laser-induced NO fluorescence pursued in this program can best be understood by reference to Figure 1, a partial energy level diagram for NO. The figure shows schematically the ground  $X^2\Pi$  electronic state and the first excited electronic state,  $A^2\Sigma^+$ . In the ground electronic state, the first seven vibrational levels are shown. Each vibrational level also contains a manifold of rotational levels which are shown schematically in  $v''=0$ .

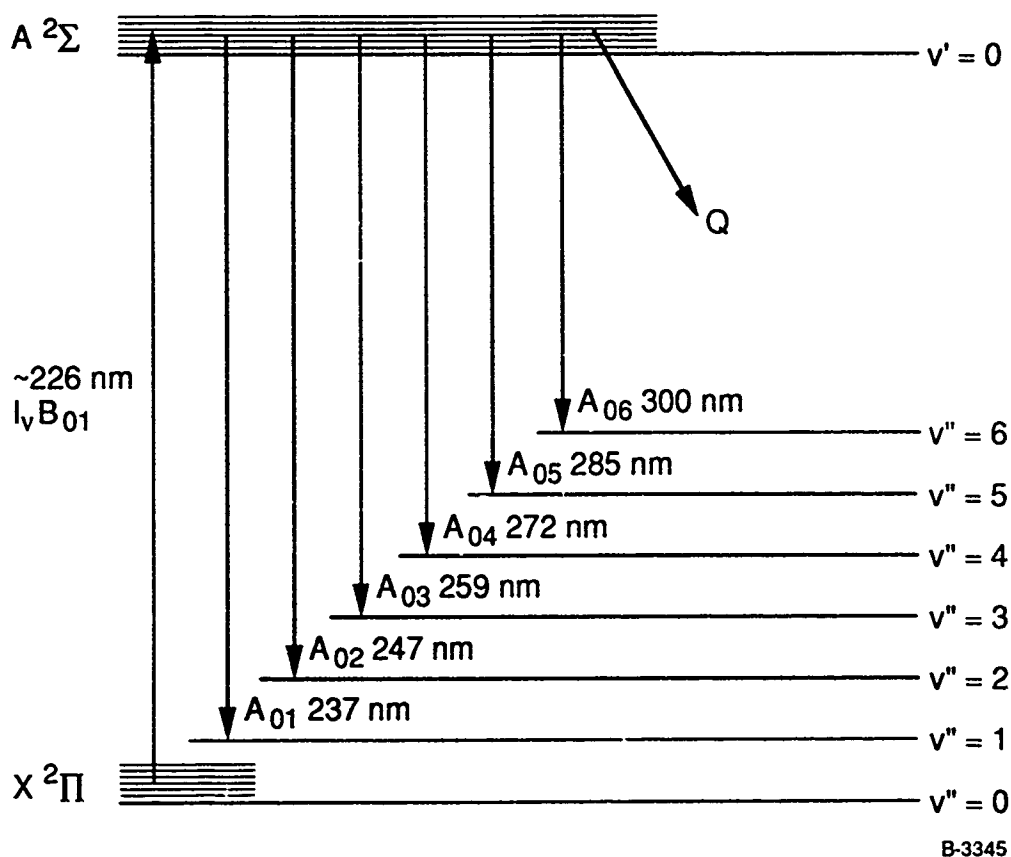


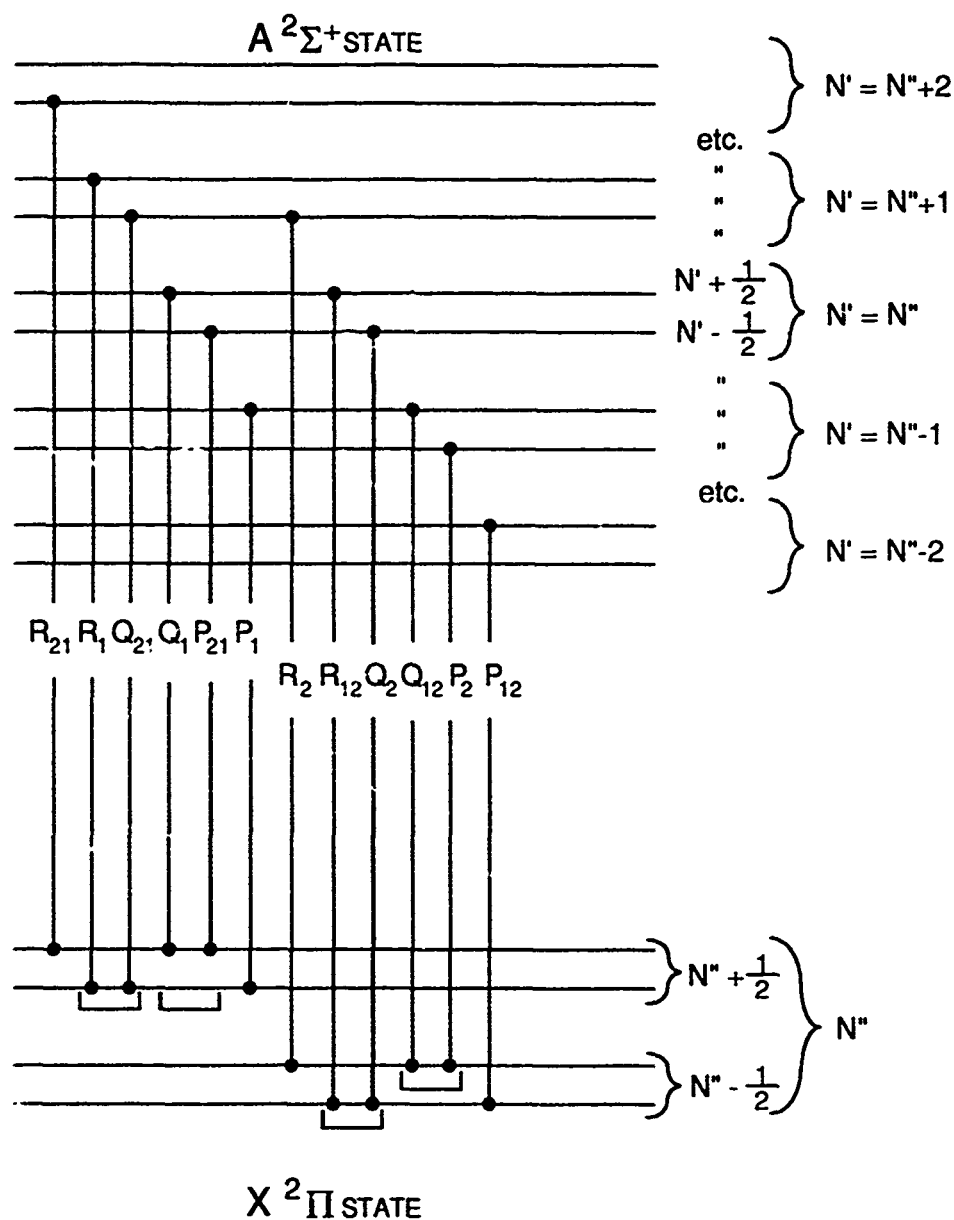
Figure 1. Schematic Energy Level Diagram Showing Important Processes in Laser-Induced NO Fluorescence

The vertical arrow at the figure left represents the energy available from a laser which is tuned to correspond to a transition from an isolated rotational level in the ground vibrational level of the lower electronic state upward to an isolated rotational level of the ground vibrational level in the upper electronic state. These rotational transitions are hereafter referred to as (0,0) band transitions, denoting the vibrational quantum numbers of the upper and lower state, respectively.

Molecules elevated to the upper electronic state may transfer to nearby rotational levels or back to the ground electronic state (the latter process is term quenching) by collisions with neighboring molecules. The quenching rate is denoted by  $Q$ . Spontaneous radiative decay competes with the collisional decay through all the allowed transition pathways from the excited state, giving rise to the fluorescence signal. Transitions from the upper electronic state to the various vibrational levels in the lower state are denoted by  $A(0,i)$ , where  $i$  represents the quantum number of the lower vibrational level.

Transitions on these off-diagonal bands shift the fluorescence to longer wavelengths and permit spectral isolation of the weak fluorescence signal from the laser wavelength. Indeed, 65 percent of the fluorescence occurs in the (0,1), (0,2) and (0,3) bands<sup>5</sup>. This aspect of our LIF approach is significant in that it permits elastic scattering of the laser radiation to be spectrally filtered, while transmitting the fluorescence. Hence, scattering from particulates, windows, or surfaces in the test facility may be efficiently discriminated.

Details of the rotational level structure in the upper and lower electronic states, along with the convention used throughout this work in labelling the rotational branches is shown in Figure 2. Each rotational level of the upper  $A^2\Sigma$  state is spin-split into two components labelled  $N' + 1/2$  and  $N' - 1/2$ , where  $N'$  refers to the rotational quantum number. Each rotational level in the lower  $X^2\Pi$  state is split by a coupling of the electronic spin and orbital angular momentum and each spin-orbit level is further split by lambda-doubling, resulting in four levels for each  $N''$ . The spin splitting in the upper state is less than 3 GHz for the highest  $N''$  transitions used in this work which is less than the transition Doppler width<sup>6</sup>.



• BRACKETS INDICATE UN-RESOLVED BRANCHES.

B-6919

Figure 2. Rotational Branches of NO A-X Transitions

Hence, transitions originating from the same lower level and terminating in each of the two spin components of the upper state are unresolved and are grouped together with brackets in Figure 2. The transition labelling employed here follows that used by Earls<sup>7</sup> for the intermediate Hunds' case in the ground electronic state.

The number of fluorescence photons collected in a single laser pulse can be expressed as

$$S_F = \int_{\omega} I_{(\omega)} g_{(\omega)} d\omega \cdot \frac{A}{A + Q} \cdot (f_B V_c N_t) \cdot \eta \frac{\Omega}{4\pi} \cdot \tau_p \quad (1)$$

where:

$I_{(\omega)}$   $\equiv$  laser spectral intensity

$g_{(\omega)}$   $\equiv$  absorption lineshape function

$A$   $\equiv$  effective radiation rate

$Q$   $\equiv$  effective quench rate

$f_B$   $\equiv$  Boltzmann population fraction in absorbing state

$V_c$   $\equiv$  collection volume

$N_t$   $\equiv$  total number density of absorbing species

$\Omega$   $\equiv$  collection solid angle

$\eta$   $\equiv$  transmissivity of collection optics

$\tau_p$   $\equiv$  laser pulse length.

The first term may be understood as an excitation efficiency, expressing the spectral overlap of the laser bandwidth and the molecular absorption bandwidth. The second term is also an efficiency: the efficiency with which an excited molecule will radiatively decay. The third term is the total population of the absorbing species in the collection volume and the final term is the fraction of fluorescence photons collected.

The velocimetry approach investigated in this work depends only on the first parenthetical term: the relative overlap of the laser spectral bandwidth and the molecular absorption bandwidth. As we explain below, the velocity measurement is always made with a ratio of two fluorescence measurements so that the remaining common terms cancel.



## 2.2 Doppler-Shifted Fluorescence

The essence of LIF velocimetry is based on the Doppler-shifted absorption frequency of an ensemble of atoms or molecules. The concept is schematically illustrated in Figure 3. A group of molecules possessing a net directed velocity, denoted by the vector  $\mathbf{v}$  is intersected by a laser beam traveling with a direction and wavelength denoted by the wave vector  $\mathbf{k}$ , both calculated with respect to a stationary reference frame (the laboratory frame). The projection of the gas velocity vector onto the laser field wave vector is given by the scalar  $u$ .

The moving gas molecules experience an optical field which is Doppler-shifted relative to an ensemble of stationary molecules. To first order, the magnitude of this Doppler-shift is given by

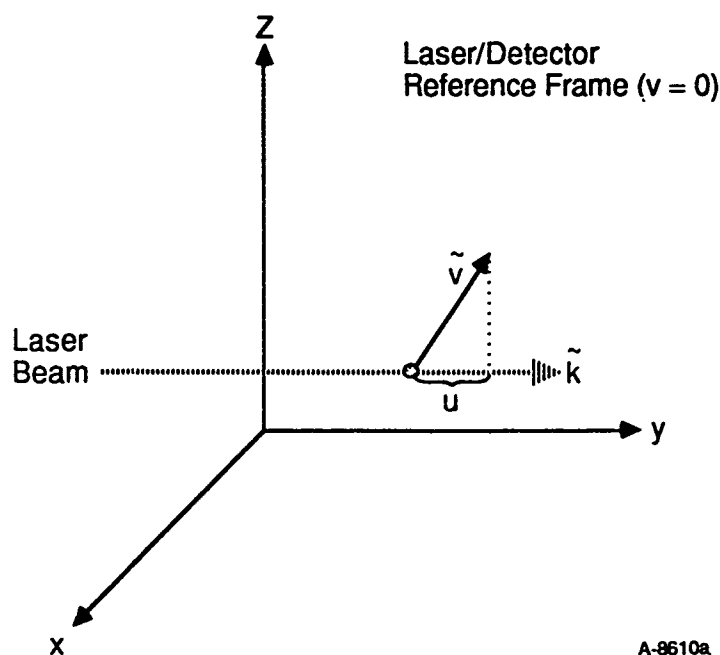


Figure 3. Schematic Illustration of the Geometry of the Linear Doppler-Shift

$$\omega_v = \omega_0 \left[ 1 \pm \frac{u}{c} \right] \quad (2)$$

where  $\omega_0$  is the zero-velocity absorption frequency and  $c$  is the velocity of light. Higher order terms due to the relativistic Doppler effect are on the order of  $(u/c)^2$  and may be neglected for practical terrestrial velocities.

The most direct measure of the magnitude of the Doppler-shift is made by scanning a laser wavelength across an absorption lineshape and determining the shift of the lineshape with respect to a stationary lineshape. This approach was first suggested by Measures<sup>8</sup> and realized by Zimmerman and Miles.<sup>9</sup> A drawback to this approach, however, is the time required to complete a stable scan of the lineshape. Most recently, a modified ring-dye laser has been scanned across OH fluorescence lineshapes in a supersonic reacting flow with an effective time resolution of approximately 1 ms.<sup>10</sup>

Because the entire absorption lineshape must be scanned, the fluorescence must be collected with a continuously recording single-point detector. Hence, it is not possible to image the velocity in a simultaneous, multi-point measurement. Finally, the narrow-band ring lasers used in these experiments are extremely sensitive research instruments requiring careful setup, constant adjustment, and are extremely sensitive to vibration, temperature changes, etc. In our view, ring-dye laser systems are unlikely to succeed as a robust test facility diagnostic system.

Examination of Eq. (1) reveals that the scanned approach is, in principle, unnecessary. Since the magnitude of the excitation efficiency overlap integral depends on the relative frequency between the laser spectral intensity lineshape and the molecular absorption lineshape, it should be possible to infer the relative velocity by a simple measure of the strength of the fluorescence signal, provided that the lineshapes of the laser and absorber are accurately known. Of course, the fluorescence signal must be normalized to account for variations in absorber number density, fluorescence efficiency, etc. This latter approach is the subject of the present program. It offers the advantage of improved time resolution and

the ability to generalize the measurement concept to single-shot, multi-point measurements using laser sheet excitation and intensified detector array fluorescence imaging.

### 2.3 Lineshape Broadening Mechanisms

Transitions between real levels in atoms and molecules do not occur at only discrete frequencies, but over a narrow range of frequencies within the absorption lineshape. The functional form of this lineshape depends on the surrounding thermodynamic state of the gas. The first broadening mechanism we consider is the thermal broadening of the lineshape due to the random motion of the molecules in the gas. The translational energy associated with the molecules results in a Maxwellian velocity distribution. Each molecule traveling with a given random velocity experiences a slightly Doppler-shifted frequency of the exciting optical field. The ensemble effect of the Maxwellian velocity distribution gives rise to the so-called Doppler profile, expressed as:<sup>11</sup>

$$g(\omega) = 2\sqrt{\frac{\ln 2}{\pi}} \frac{1}{\Delta \omega_D} \exp\left[-4 \ln 2 \frac{(\omega - \omega_0)^2}{\Delta \omega_D^2}\right] \quad (3)$$

where:

$\Delta \omega_D \equiv$  Doppler-width

and is given by

$$\Delta \omega_D = 2 \left[ \frac{2 kT \ln 2}{mc^2} \right]^{1/2} \omega_0 \quad (4)$$

$\omega_0 \equiv$  frequency of the absorption line-center .

If Doppler-broadening were the only broadening mechanism of relevance, the lineshape would depend on a single parameter of the surrounding flowfield - the temperature.

Near atmospheric pressure, however, a second broadening mechanism is important. Collisions with neighboring molecules interrupt the coherent interaction of the molecule with

the optical field and perturb the energy levels of the molecule, introducing the so-called Lorentz lineshape<sup>12</sup>

$$g(\omega) = \frac{\Delta\omega_c}{2\pi(\omega-\omega_s)^2 + \frac{\pi}{2} \Delta\omega_c^2} \quad (5)$$

where  $\omega_s$  is the shifted line center absorption frequency and  $\Delta\omega_c$  is the collision-width. The collisional shift arises from the perturbation of the isolated molecular energy levels during the collision. It is typically expressed as a fraction of the collision width

$$\omega_s = \omega_0 + \beta\Delta\omega_c \quad (6)$$

where  $\beta$  may be positive or negative, depending on the structure of the electronic orbitals of the colliding species.

The simultaneous action of both collisional and Doppler-broadening results is expressed as a convolution of the two profiles. The resultant expression is the well known Voigt profile

$$g(\omega) = \left[ \frac{mc^2}{2\pi kT} \right]^{1/2} \left[ \frac{\Delta\omega_c}{2\pi\omega_0} \right] \int_{-\infty}^{\infty} \frac{\exp \left[ \frac{-mc^2(\omega' - \omega_s)^2}{2kT \omega_0^2} \right]}{[(\omega - \omega_s) - (\omega' - \omega_s)]^2 + \left[ \frac{\Delta\omega_c}{2} \right]^2} d\omega' \quad (7)$$

This is usually written in terms of the Voigt function

$$g(\omega) = \frac{2\sqrt{\ln 2}}{\sqrt{\pi} \Delta\omega_D} V(\xi, a) \quad (8)$$

where:

$$V_{(\xi,a)} \equiv \frac{a}{\pi} \int \frac{\exp(-y^2)}{a^2 + (\xi-y)^2} dy \quad (9)$$

and

$$\xi = 2\sqrt{\ln 2} \left[ \frac{\omega - \omega_s}{\Delta\omega_D} \right]$$

$$y = 2\sqrt{\ln 2} \left[ \frac{\omega' - \omega_s}{\Delta\omega_D} \right]$$

$$a = \sqrt{\ln 2} \left[ \frac{\Delta\omega_c}{\Delta\omega_D} \right]$$

The Voigt "a-parameter" is thus a measure of the relative contribution of collisional and Doppler broadening to the absorption lineshape. Since the probability for transition integrated over the entire lineshape must remain unchanged in the presence of broadening mechanisms, the integral of the lineshape over all frequencies is equal to unity.

While the Doppler-width for a given transition is easily calculated, the collisional-width and -shift are more problematic. Physically, the width is simply proportional to the rate of broadening collisions. As such, it is dependent on the composition of the surrounding gas, the overall gas pressure, and temperature. The pressure dependence is usually separated by expressing the collision width as<sup>12</sup>

$$\Delta\omega_c = \frac{1}{2\pi c} \sum_i 2\gamma_i P_i \quad (10)$$

where  $\gamma_i$  is the collision broadening parameter for species  $i$ ,  $P_i$  is the partial pressure of species  $i$ , and the summation is over all available collision partners. The temperature dependent collisional broadening parameter may vary with the particular transition involved, as well as the surrounding gas.

### 3. HIGH-RESOLUTION MEASUREMENTS OF NO LINESHAPE PARAMETERS

Few measurements are available of the collisional broadening parameters for NO. Prior to this study, the only broadening measurements available were a set of room temperature measurements made using spectrally-resolved flashlamp absorption measurements.<sup>13</sup> The resolution of this approach is not high so that the inferred broadening is questionable and no temperature-dependent data was available. As shown in the preceding sections, the velocity measurement technique depends sensitively on the detailed absorption lineshape, it is necessary to accurately measure the temperature-dependent collisional broadening and shift for various collisional partners relevant to high-temperature aerodynamics such as O<sub>2</sub>, H<sub>2</sub>O, N<sub>2</sub>, and NO self-broadening.

The most accurate approach for detailed lineshape measurements is based upon laser-absorption measurements using a source whose spectral bandwidth is much less than the inherent linewidth to be measured. The wavelength of this source is tuned across the lineshape and the resultant absorption signature accurately reflects the lineshape at the measurement temperature, pressure, and collisional environment. The ability to generate tunable, ultra-narrow frequency laser radiation at wavelengths shorter than 260 nm is not generally available and, in the interest of efficiency, we elected to subcontract NO lineshape measurements to Stanford University, which has developed a unique laser source.

A Coherent 699 ring dye laser was run with Stilbene 420 dye and pumped with 6W (all lines UV) from a Coherent Innova 25/5 Ar<sup>+</sup> laser. Using a custom-designed intra-cavity BBO tuning assembly, 3 mW of continuous, single-mode laser radiation was generated in the vicinity of 225 nm. Tuning was affected using another custom-designed intra-cavity scheme. This consisted of removing the standard etalon and Brewster plate assembly and inserting a pair of Brewster-angle-cut fused-silica rhombs in front of the visible output coupler. The rhombs were mounted on a magnesium platform and driven by a galvanometer assembly at its resonant frequency of 2 kHz. With this approach, the single mode output of the laser (spectral bandwidth  $\sim 1$  MHz) could be scanned continuously over 2 to 3 cm<sup>-1</sup>. Said



laser scan. The UV output from the laser was focussed through a static cell containing less than 1 percent NO and various background pressures of N<sub>2</sub>. A portion of the UV beam was directed onto a photodetector before entering the cell and a second detector recorded the transmitted intensity.

The attenuation of the laser beam is described by the Beer-Lambert relation

$$\frac{I}{I_0} = \exp \left( - \int \alpha(\omega) dx \right) \quad (11)$$

where:

$\alpha(\omega) \equiv$  spectral absorbance at  $\omega$

$x \equiv$  spatial extent of absorption.

The spectral absorbance is directly proportional to the number density of absorbers and, more importantly for our application, to the absorption lineshape function derived in Subsection 2.3. A fourth detector was used to measure the laser-induced fluorescence from a portion of the beam near the center of the cell. A comparison of the lineshapes inferred from both absorption and fluorescence in this scheme provides a measure of the quality of data with respect to saturation or optical thickness.

Figure 5 shows the output from the four detectors as a function of time during a series of typical scans. Each trace was recorded using a four-channel Nicolet 4094 oscilloscope sampling at 2 MHz. The top trace is the incident laser intensity which varies during the course of a scan due to phase-matching variations in the fixed-angle BBO crystal. The bottom trace is the difference between the output of the transmitted beam detector and the incident beam detector, which is proportional to the absorption lineshape. The third trace is the output from the fluorescence monitoring PMT, also proportional to the absorption lineshape. The bottom trace is the transmission through the visible etalon which provides fiducial marks at fixed frequency spacings as a function of time. (Note that, although the scan rate is not a linear function of time, the etalon output provides the correction factor.)



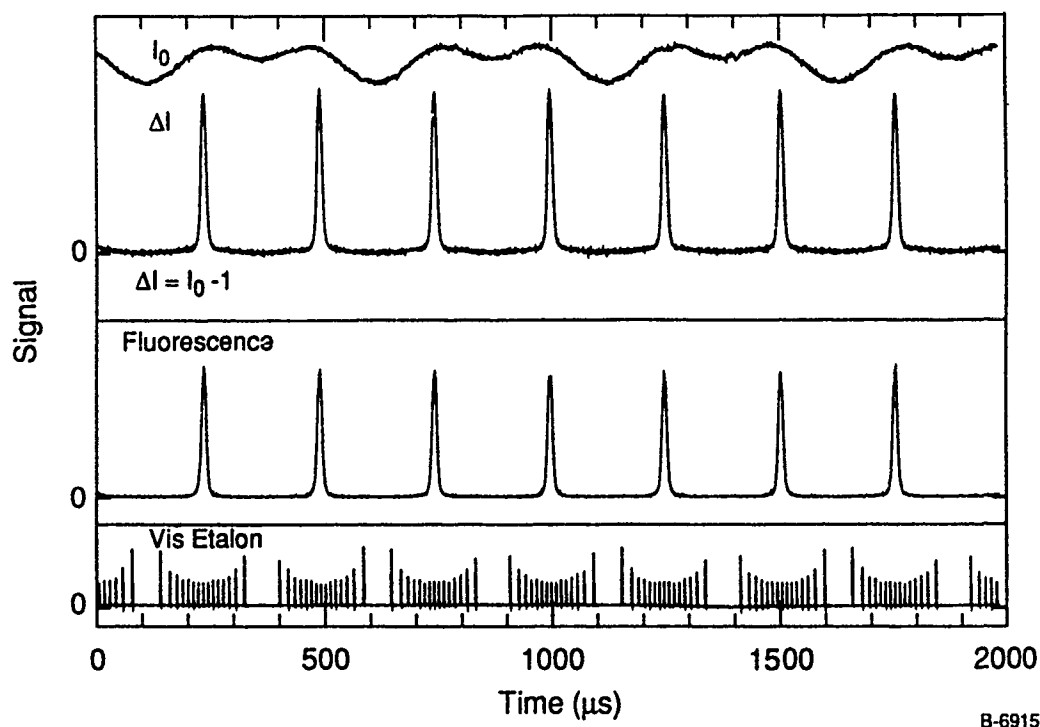


Figure 5. Absorption and Fluorescence Data Traces from High Resolution Static Cell Measurements

Figure 6 is the reduced absorption lineshape function, normalized to unity at the line-center, of the isolated  $P_2(13)$  feature at 226.7562 nm. The lineshape was recorded at 294 K with a cell pressure of 48 torr  $N_2$  and 0.4 percent NO. The experimental data points are shown together with a least squared-error fit Voigt profile. In this fit, the only adjustable parameter is the collisional broadening parameter of Eq. (10), which was determined to be  $0.29 \text{ cm}^{-1} \text{ atm}^{-1}$ . This measurement allows extraction of the a-parameter for NO- $N_2$  broadening at 300 K, which was determined to be 0.31 for this measurement. The lower trace is the residual difference between the Voigt fit and the experimental data and shows that the maximum deviations are less than 2 percent.

The slight asymmetry in the residual plot is the result of neglecting higher-order models of collision broadened lineshapes which include asymmetric broadening processes. The simplest of these higher order fits is described by a Galatry profile.<sup>15</sup> Similar traces at

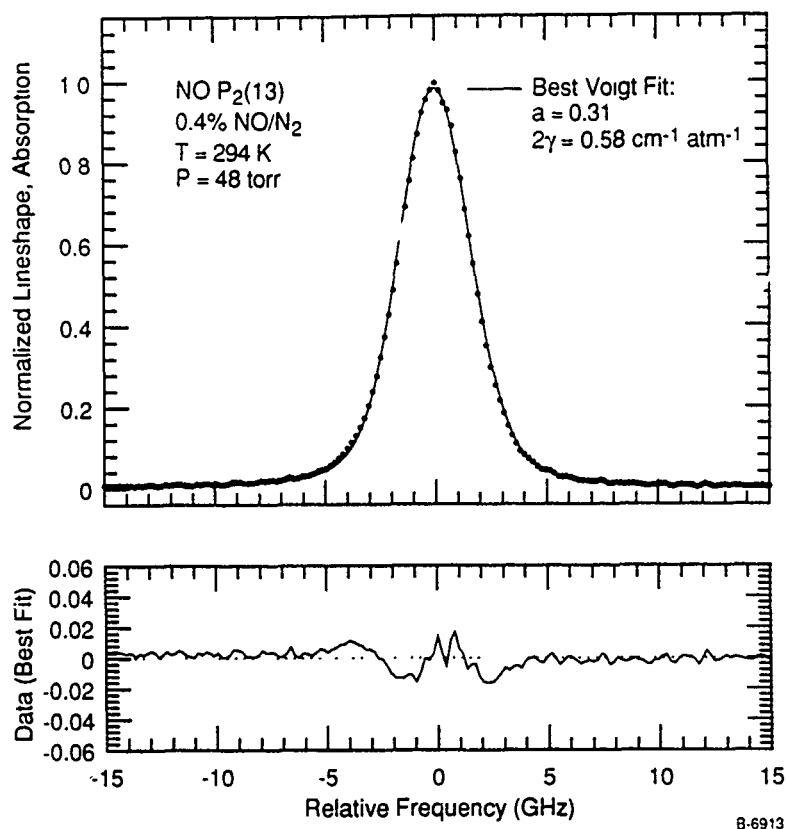


Figure 6. NO Absorption Lineshape Measurement

pressures up to 0.7 atm suggests that the collisional asymmetry remains a minor contribution to the overall lineshape and can be neglected for the present purpose.

By recording similar traces at various  $N_2$  background pressures, it was possible to determine the frequency-shift of the line-center frequency. Hence, the collisional shift was measured to be

$$\frac{\Delta\omega_s}{\Delta\omega_c} = -0.303 \quad . \quad (12)$$

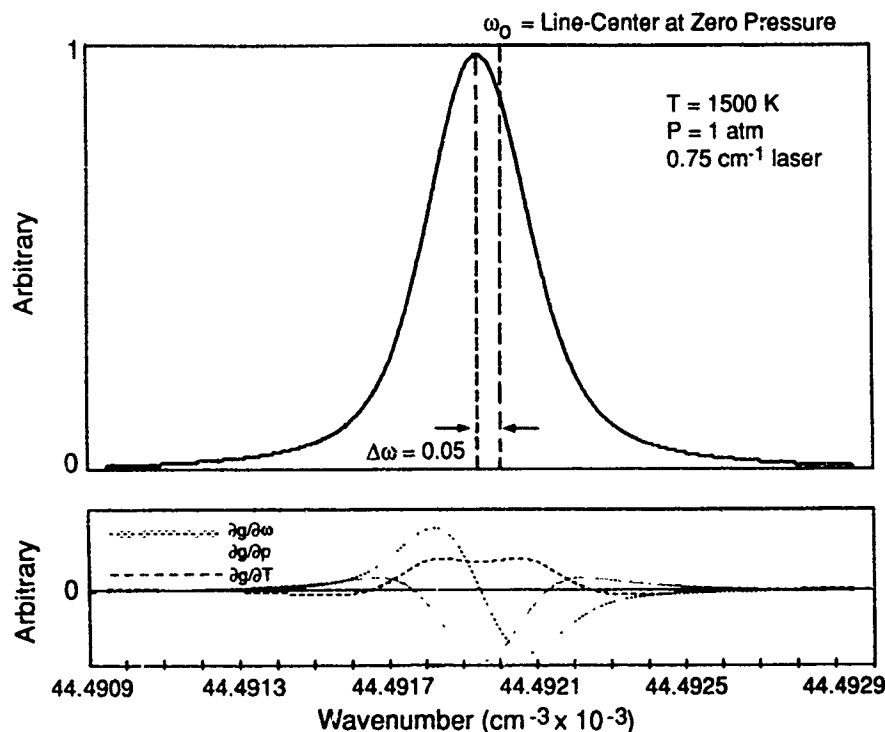
The shift/width ratio is expected to be independent of temperature.

In a more extensive series of temperature-dependent measurements in a shock-tube using dilute NO-Ar mixtures, DiRosa, et al.,<sup>14</sup> report the following expression for the a-parameter temperature variation:

$$a = 4180 PT^{-1.2} \quad (13)$$

Because such complete data for  $N_2$  was not available, we used this expression to evaluate the a-parameter in all our analytical modelling along with the constant shift/width ratio of Eq. (12).

An example of an isolated NO lineshape which would be recorded by the much broader pulsed dye lasers to be used in the velocimeter is shown in Figure 7, a calculation of the  $Q_1(33)$  fluorescence lineshape at 1 atm and 1500 K.



B-6914

Figure 7. An NO Voigt Lineshape for the  $Q_1(33)$  Transitions and Its Derivatives

The laser lineshape was modelled as a Gaussian with a full-width at half-maximum of  $0.75 \text{ cm}^{-1}$ . The Voigt functions were calculated using a rational approximation to the complex probability function as derived by Humlicek<sup>16</sup> and checked against the tabulations of Armstrong.<sup>17</sup> The magnitude of the collisional shift at this pressure is  $0.05 \text{ cm}^{-1}$ . The lower panel shows the derivative of the lineshape with respect to frequency, temperature, and pressure. The derivatives are each plotted against separate, arbitrary scales for visualization: in fact, the value of the temperature derivative is less than a few percent of the pressure and frequency derivatives.

Inspection of the Voigt derivatives is instructive, particularly from the point of view of determining the sensitivity of the convolution lineshape to temperature, pressure, and frequency changes. Near the line center, the magnitude of the absorption lineshape is particularly sensitive to pressure: increases in pressure tend to depress the lineshape value due to overall broadening of the lineshape. Also at line center, the derivative of the lineshape with respect to frequency crosses zero. In this region of the lineshape, the magnitude of the laser linewidth/absorption linewidth overlap (proportional to the excitation efficiency) is least sensitive to small changes in the relative frequency between the laser line center and the molecular absorption line center. Thus, the excitation efficiency is relatively insensitive to velocity when the overlap is concentrated in the vicinity of the absorption line center frequency.

Away from line-center, the sensitivity of the lineshape to changes in frequency (and, hence, Doppler-shifts in the relative frequency due to directed velocity) increases, reaching a broad maximum near the full-width, half-maximum (FWHM) of the absorption lineshape. Coincidentally, near this same region, the derivatives of the lineshape with respect to temperature and pressure are near zero. Thus, in this region of the absorption lineshape, the magnitude of the overlap integral is most sensitive to small relative velocity changes and least sensitive to changes in flow temperature and pressure.

## 4. ANALYTICAL STUDY OF VELOCITY ALGORITHMS

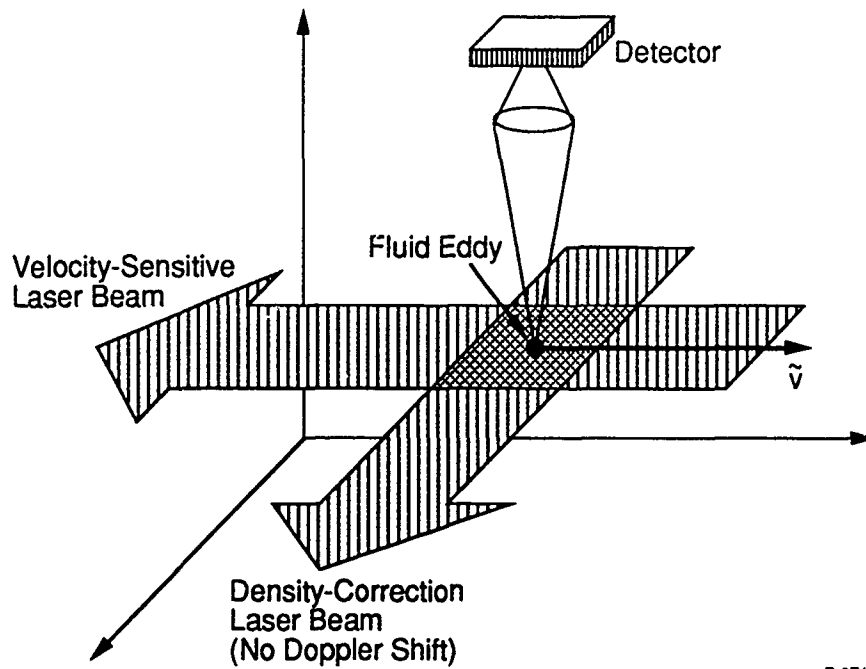
This section presents results from a detailed analytical study of the LIF velocimetry approach. The goal of the study was a quantitative understanding of the uncertainty in the inferred velocity due to pressure and temperature variations in the flowfield across the measurement plane as well as uncertainties introduced by laser bandwidth fluctuations and signal noise considerations. Temperature and pressure variations are particularly important in compressible flow applications where duct cross-section changes, shock waves, or combustion-generated heat release may be expected to significantly modify these fields through the system. Since the ultimate goal of the technique is multiple-point velocity imaging, it is important to examine the sensitivity to these flowfield variations in the measurement plane. Practical experimental considerations such as laser bandwidth stability and signal noise may also be limitations to accurate velocity measurements, particularly in PLIF measurements where the signal shot-noise levels may be large.

### 4.1 Derivation of Velocity Algorithms

The form of the algorithm derived to determine the flow velocity from LIF measurements depends primarily on two criteria:

1. The dimensionality of the velocity field
2. The relative magnitude of the laser spectral bandwidth ( $\Delta\omega_L$ ) and the molecular absorption bandwidth ( $\Delta\omega_A$ ).

We will begin this section with the simplest case of a one dimensional flowfield, i.e.,  $v_i \rightarrow v$ . Such a flowfield might be found at the inlet plane of a vitator-driven tunnel, for example. Although not strictly required, it is useful pedagogically to first assume that optical access is available both along the flow direction (velocity sensitive) and perpendicular to the flow direction (no velocity sensitivity). This experimental arrangement is illustrated in Figure 8.



B-3746

Figure 8. Schematic Diagram of Optical Access for One-Dimensional Flow Measurements

The magnitude of the fluorescence signal determined by the laser beam crossing the flow axis is denoted by  $S_{F1}$  where

$$S_{F1} \sim \int I_{(\omega)} g(\omega) d\omega \quad (14)$$

Similarly, the magnitude of the fluorescence from the laser beam propagating along the flow axis is given by

$$S_{F2} \sim \int I_{(\omega)} g(\omega - \omega_v) d\omega \quad (15)$$

where  $\omega_v$  is the Doppler-shifted frequency given by Eq. (2).

In order to derive simple, closed-form expressions for the velocity as a function of the fluorescence signal, it is necessary to make some assumptions regarding the relative width of

the laser spectral bandwidth and the molecular absorption lineshape,  $g(\omega)$ . Heuristically, it is convenient to first assume that the laser spectral bandwidth is much smaller than the molecular absorption lineshape. This is schematically illustrated in Figure 9, which shows the two functions plotted against frequency. The magnitude of the overlap integral is indicated by the hatched region.

In this limit, we may replace the laser spectral bandwidth with a delta-function in frequency and write

$$I(\omega) = I\delta(\omega - \omega_L) \quad (16)$$

where:

$\omega_L$  = laser line-center frequency

and the normalization of the delta function is such that

$$\int I\delta(\omega - \omega_L)d\omega = I \quad (17)$$

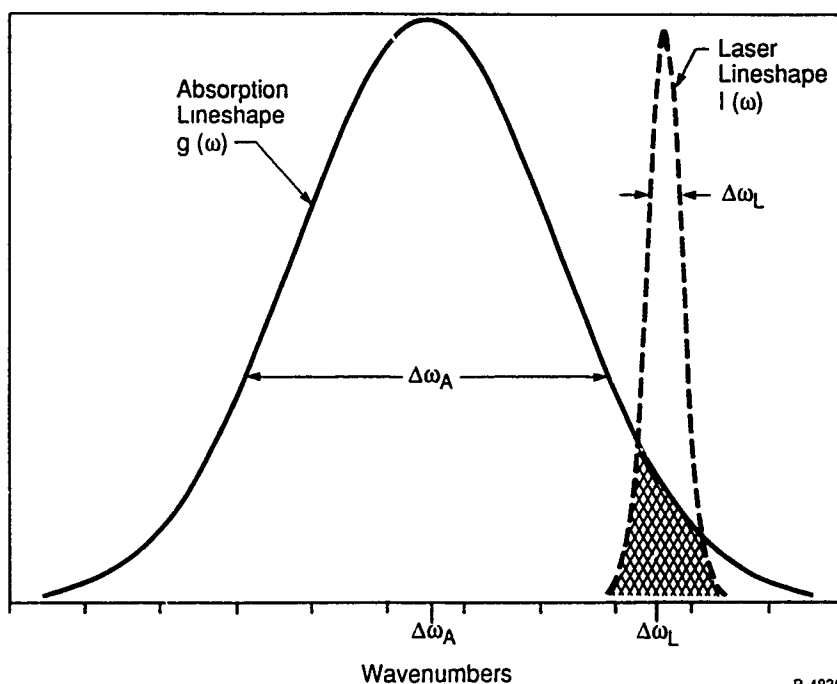


Figure 9. Molecular Absorption Lineshape and Laser Spectral Bandwidth Overlap for a Narrow-Bandwidth Laser

Substituting Eq. (16) into Eqs. (14) and (15) gives

$$S_{F1} = I g(\omega_L) \quad (18)$$

and

$$S_{(F2)} = I g(\omega_L - \omega_v) \quad (19)$$

Expanding the velocity-shifted lineshape function,  $g(\omega_L - \omega_v)$ , in a Taylor Series about  $\omega_L$  and retaining only the linear term gives

$$g(\omega_L - \omega_v) = g(\omega_L) + \frac{\partial g}{\partial \omega}(\omega_L - \omega_v) \quad (20)$$

Using Eq. (20) to replace the Doppler-shifted lineshape function in Eq. (19) yields the following form for the fluorescence ratio:

$$\frac{S_{F2}}{S_{F1}} = 1 + \frac{\left. \frac{\partial g}{\partial \omega} \right|_{\omega_L}}{g(\omega_L)} (\omega_L - \omega_v) \quad (21)$$

Substituting for the doppler-shifted frequency,  $\omega_v$ , and inverting yields the following expression for the flow velocity as a function of the fluorescence ratio:

$$V = \frac{c}{\omega_L} \left( 1 - \frac{S_{F2}}{S_{F1}} \right) \frac{g(\omega_L)}{\left. \frac{\partial g}{\partial \omega} \right|_{\omega_L}} \quad (22)$$

In this case, the velocity algorithm is sensitive to the inverse of the slope of the molecular absorption lineshape normalized by the magnitude of the lineshape. As discussed above, these quantities are sensitive to the local temperature and pressure, depending on the exact frequency of the laser relative to the molecular lineshape center frequency. This basic approach was used by Hiller, et al.<sup>18-20</sup> in the early LIF velocimetry literature. Their approach was to seed the flow with molecular iodine and probe the fluorescence using a frequency modulated  $\text{Ar}^+$  laser.



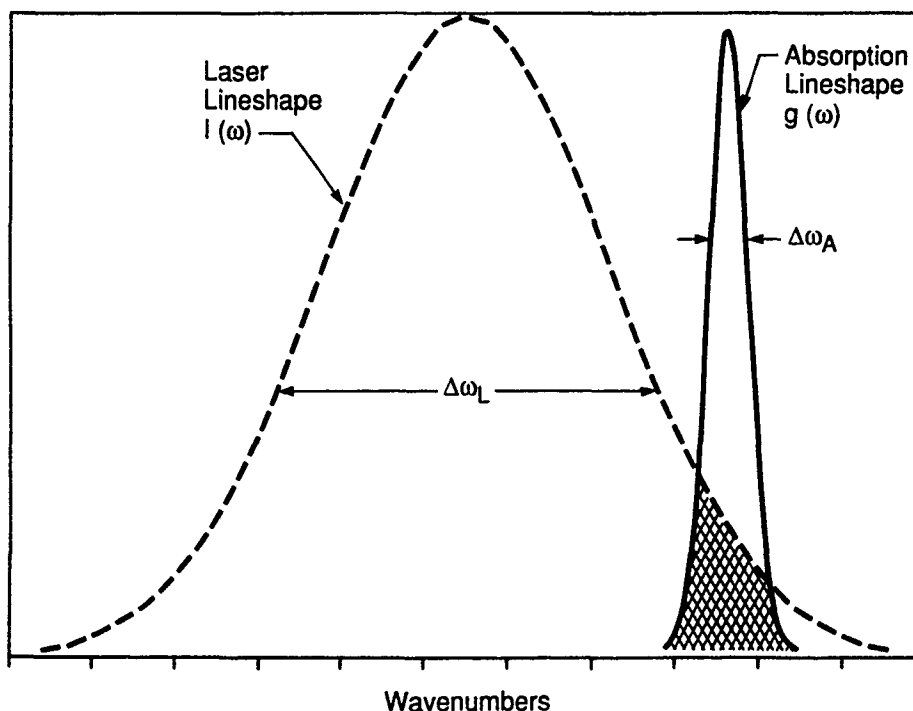
In their work, the sensitivity of the molecular absorption lineshape proved a barrier to quantitative measurements. It was necessary to use two separate laser wavelengths (derived from acousto-optic modulation of the  $\text{Ar}^+$  frequency) in order to make a two-point estimate of the slope of the lineshape. Specific laser excitation frequencies were chosen in order to minimize the pressure and temperature sensitivity of this two-point slope estimate. Because the algorithm depended only on the linear term of the linewidth expansion, it was necessary to restrict the range of velocity shifts such that the range of frequencies fell within the linear slope of the molecular absorption lineshape.

The opposite limiting case is found when the laser spectral bandwidth is much larger than the molecular absorption lineshape, schematically illustrated in Figure 10. In this limit, the molecular absorption lineshape is expressed in terms of a delta-function

$$g(\omega) = g\delta(\omega - \omega_A) \quad (23)$$

where:

$\omega_A \equiv$  absorption line-center.



8-4837

Figure 10. Molecular Absorption Lineshape and Laser Spectral Bandwidth for a Broad-Bandwidth Laser

By expanding the laser lineshape in a Taylor Series and following the same procedure as before, the following expression is derived:

$$V = \frac{c}{\omega_A} \left( 1 - \frac{S_{F2}}{S_{F1}} \right) \frac{I(\omega_A)}{\left. \frac{\partial I}{\partial \omega} \right|_{\omega_A}} . \quad (24)$$

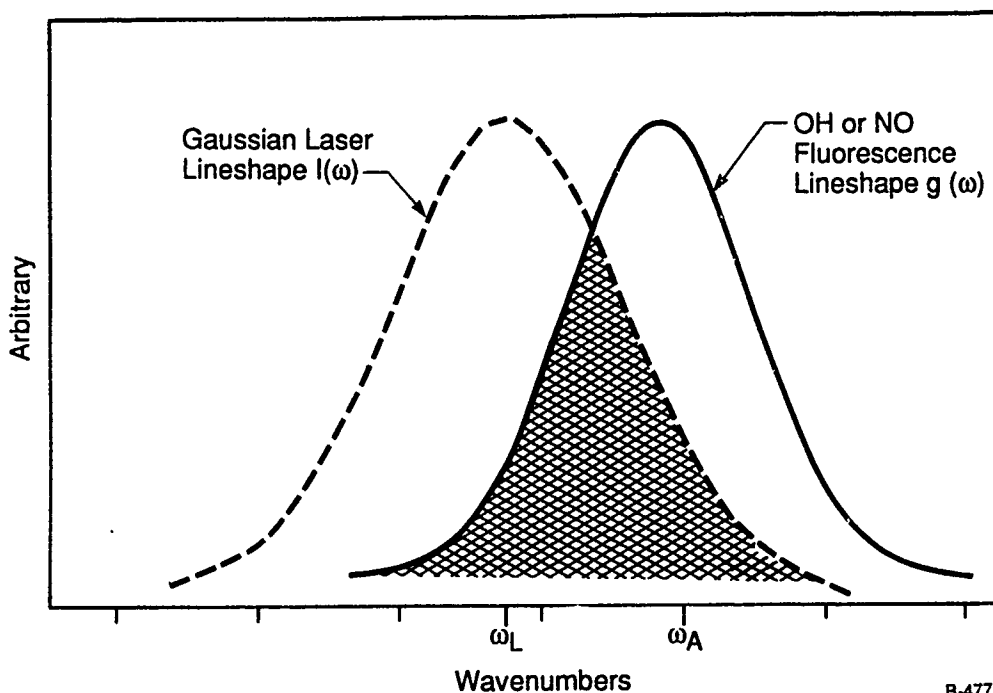
Equation (24) is analogous to Eq. (22) except that the normalized lineshape in the algorithm is now the laser lineshape rather than the molecular absorption lineshape. This is convenient since the algorithm is now independent of flow temperature and pressure fluctuations and is only a function of the laser spectral properties. This approach was used by Paul et al.,<sup>21</sup> to measure the velocity distribution in a cold, supersonic jet seeded with NO. In this case, the low temperature and pressure of the flow collapsed the absorption lineshape and a broadband pulsed dye laser was used to excite the fluorescence.

While an attractive approach for low pressure, low temperature flowfields, the broadband laser limit is generally not achievable with commercially available pulsed dye lasers in applications near atmospheric pressure. Most pulsed dye lasers operate with spectral bandwidths (without intra-cavity etalons for bandwidth narrowing) between  $0.3 \text{ cm}^{-1}$  and  $0.8 \text{ cm}^{-1}$  when frequency-doubled into the UV. By comparison, typical NO linewidths near atmospheric pressure and 1500 K are  $0.3 \text{ cm}^{-1}$ . Hence, neither limiting condition described above can apply.

In the intermediate case, illustrated in Figure 11, there is not a simple, closed form expression for the velocity as a function of the ratio of the fluorescence signals. Rather, we define an implicit velocity algorithm,  $\psi(v)$ , as follows:

$$\psi(v) \equiv \frac{S_{F2}}{S_{F1}} = \frac{\int I(\omega) g(\omega - \omega_v) d\omega}{\int I(\omega) g(\omega) d\omega} . \quad (25)$$

We now generalize our basic approach to the case of non-directed flows. As pointed out by Hiller,<sup>20</sup> it is not necessary that one of the fluorescence measurements be directed



B-4773

Figure 11. Molecular Absorption Lineshape and Laser Spectral Bandwidth Overlap for Equivalent Bandwidths

across the flow with no Doppler-shift. Using counter-propagating beams, up-shifted and down-shifted by the same magnitude, it is possible to derive similar velocity expressions. We denote the up-shifted values as  $S_{F+}$  and the down-shifted values as  $S_{F-}$ . For the case of the narrow-bandwidth laser, the form of the velocity algorithm derived according to the procedure described above is

$$V = \frac{c}{\omega_L} \left[ \frac{2S_{F+}}{S_{F+} + S_{F-}} - 1 \right] \frac{g(\omega_L)}{\left. \frac{\partial g}{\partial \omega} \right|_{\omega_L}} \quad (26)$$

Similarly, for the broad-bandwidth laser, the form of the algorithm is

$$V = \frac{c}{\omega_L} \left[ \frac{2S_{F^+}}{S_{F^+} + S_{F^-}} - 1 \right] \frac{I_{(\omega_A)}}{\left. \frac{\partial I}{\partial \omega} \right|_{\omega_A}} \quad (27)$$

In each case, it is only the premultiplier of the normalized slope which is different from the expressions derived from the directed flow cases. Hence, it is possible to determine a single component of the velocity field with optical access at an arbitrary angle to the field. The component so derived will always be aligned with the counter-propagating beam paths.

In the intermediate case, again, no simplification of the overlap integral is possible and the form of the velocity algorithm is given by

$$\psi(v) = \frac{\int I(\omega)g(\omega+\omega_v)d\omega - \int I(\omega)g(\omega-\omega_v)d\omega}{\int I(\omega)g(\omega+\omega_v)d\omega + \int I(\omega)g(\omega-\omega_v)d\omega} \quad (28)$$

In summary, this section has shown how the LIF velocimetry approach may be sensitive to the temperature and pressure of the flowfield due to the variations in the normalized slope of the molecular absorption lineshape, depending on the relative magnitude of the laser spectral bandwidth and the molecular absorption lineshape. As the laser spectral bandwidth increases, the sensitivity of the overlap to details of the fluctuation of the molecular absorption bandwidth is diminished. The following section discusses the magnitude of the overlap integral as a function of flow velocity for variable temperature, pressure, and laser spectral bandwidth.

#### 4.2 Pulsed Laser Excitation Scans

Equation (28) shows that the implicit velocity algorithm is the ratio of a difference and a sum of two points on the convolution of the laser lineshape and the molecular absorption lineshape. For a given velocity shift, two points on the convolution lineshape are subtracted from one another and this difference is normalized by their sum. Hence, a laser

excitation scan of the fluorescence spectrum of a gas at rest provides the functional form from which points are extracted in the velocity algorithm if the flow is accelerated.

In order to identify appropriate transitions to be used in the velocimeter and to understand the effect of the spectrally broad pulsed dye laser on the absorption lineshapes, a series of excitation scans were conducted in a static cell, according to the setup shown in Figure 12. Tunable UV laser light was generated using a Lambda-Physik FL 3002 dye laser pumped by an LPX 210i XeCl excimer laser. The output from Coumarin 450 dye was extra-cavity frequency doubled in a single pass through an angle-tuned, temperature-stabilized BBO crystal. Computer control synchronized the rotation of the dye laser grating with the crystal angle so that continuous scans over  $\sim 3$  nm were possible with pulse energies of 2 to 4 mJ. The laser light was directed through a cell (unfocussed) in which various pressures of air and NO could be introduced.

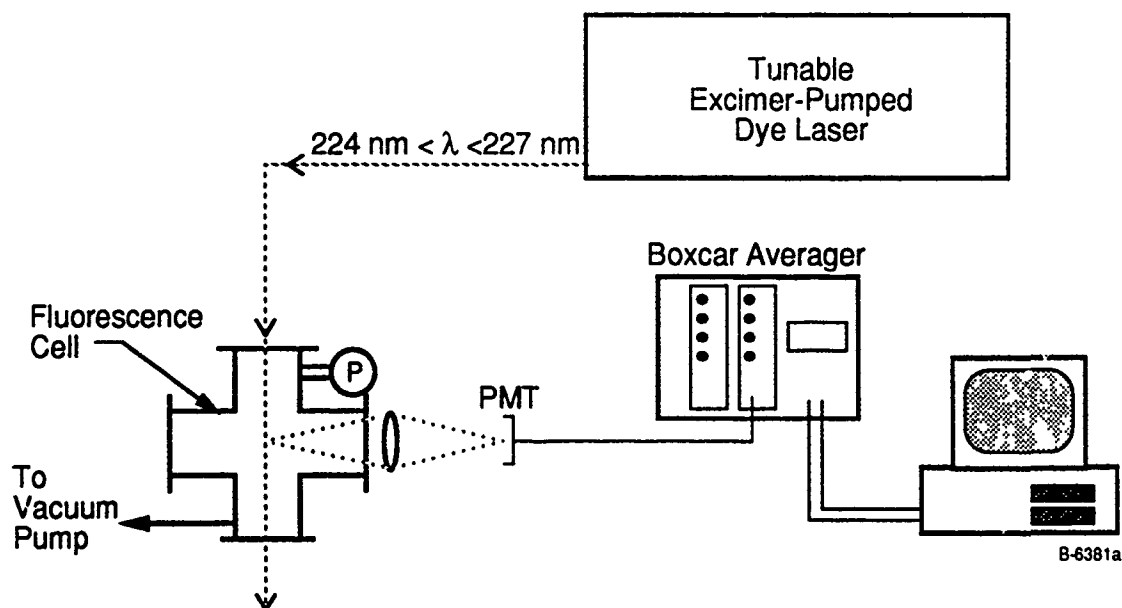


Figure 12. Experimental Setup for Pulsed Laser Excitation Scans

The laser was operated at repetition rates between 10 and 60 Hz. Fluorescence was collected with a Hamamatsu R/955 PMT and averaged over 10 to 30 laser pulses using a Stanford Research Systems Gated Integrator and Boxcar Averager. The laser scan time was adjusted so that the laser wavelength was stationary during the 1 to 3 s integration time of the boxcar averager. The averaged fluorescence signal was recorded on a laboratory computer.

An example of the data obtained in these experiments is shown in Figure 13, a portion of a room temperature excitation scan taken at  $P < 1$  torr in a sealed cell. The  $P_{12}$  bandhead at 227 nm is labelled, along with portions of the  $P_2$ ,  $Q_2$ , and  $R_2$  branches. The linewidths of these fluorescence features are largely determined by the  $\sim 0.75 \text{ cm}^{-1}$  laser bandwidth since the inherent Doppler width at 300 K is  $0.098 \text{ cm}^{-1}$ . At higher temperatures, this portion of the NO spectrum is poorly resolved and therefore unsuitable for velocimetry applications.

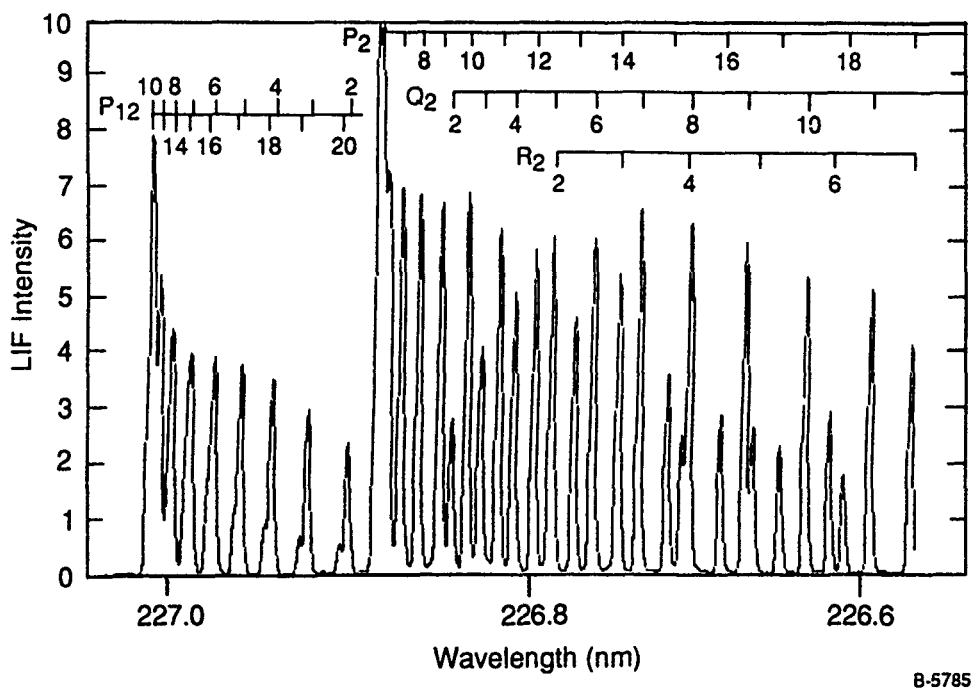


Figure 13. Room Temperature NO Pulsed Laser Excitation Scan

A more detailed portion of the spectrum is shown in Figure 14, showing the region between 224.68 and 224.84 nm. The figure shows room temperature data in the dashed line along with a predicted spectrum for a  $0.75\text{ cm}^{-1}$  bandwidth Gaussian laser profile. The spectral agreement for the lower  $N''$  values is excellent because the computer simulated spectrum uses observed line positions where available. At higher rotational quantum numbers, the spectral simulation code predicts the transition wavelength using a Dunham coefficient expansion.<sup>22</sup> The expansion is accurate to within about 1/3 of the convolution linewidth, as seen in the figure. From this fit, and a similar fit taken with 1 atm background air pressure to check for saturation effects, the mean laser bandwidth is determined to be  $0.75\text{ cm}^{-1}$ , in good agreement with the dye laser specifications. The experimental trace also serves to verify the accuracy of the spectral generating code, allowing spectra to be simulated at conditions more relevant to the proposed instrument.

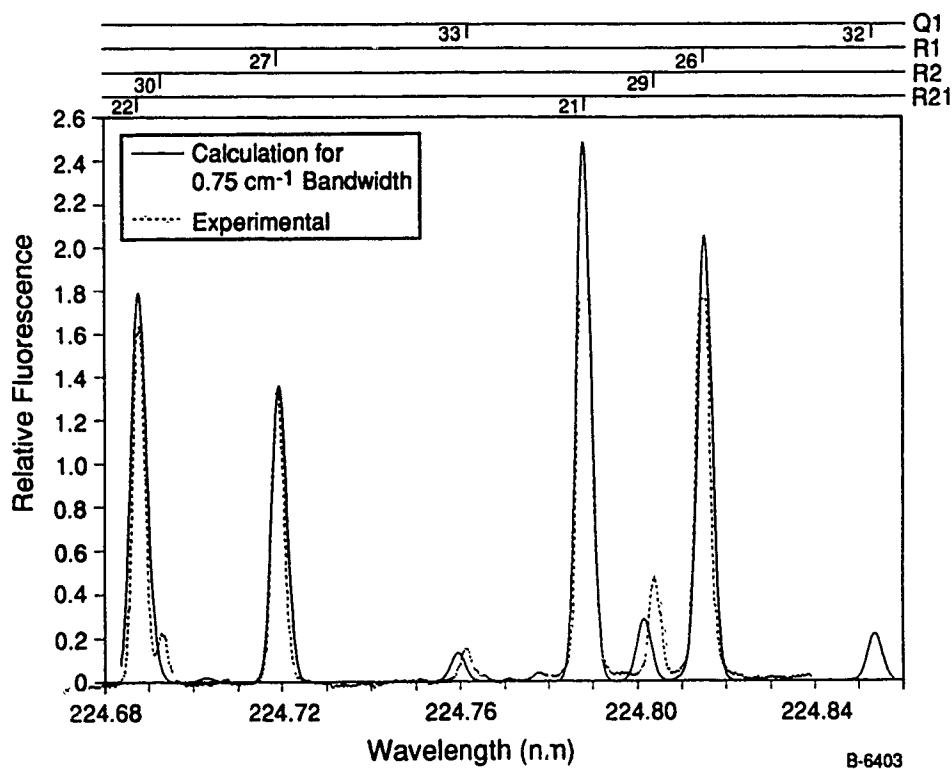


Figure 14. NO Excitation Scan Detail - 300 K

Figure 15 shows a calculated absorption and excitation spectrum for the same wavelength range, now at 1500 K and 1 atm air. The broadening was calculated using the a-parameter fit of Eq. (13). The dotted line is the actual absorption spectrum and the solid line is the convolution spectrum with the  $0.75 \text{ cm}^{-1}$  bandwidth laser. Recall that the velocity algorithm is derived from ratios of points along the solid line. Whereas the  $Q_1(33)$  line was very weak in Figure 14, due to the relatively low temperature there, it is a strong, well-isolated feature in Figure 15. Extensive survey of high temperature excitation spectral simulations revealed that of the  $\sim 300$  strong transitions at these temperatures, only a few transitions of the  $Q_1$  branch in the vicinity of  $N'' = 33$  were sufficiently isolated from one another to ensure that contributions from neighboring lines did not complicate the data reduction. At wavelengths below 224.65 nm, (1,1) band transitions overlap the (0,0) band transitions of interest here. Hence, the  $Q_1(33)$  line was used as the candidate transition in all of the modelling and signal strength analyses to follow.

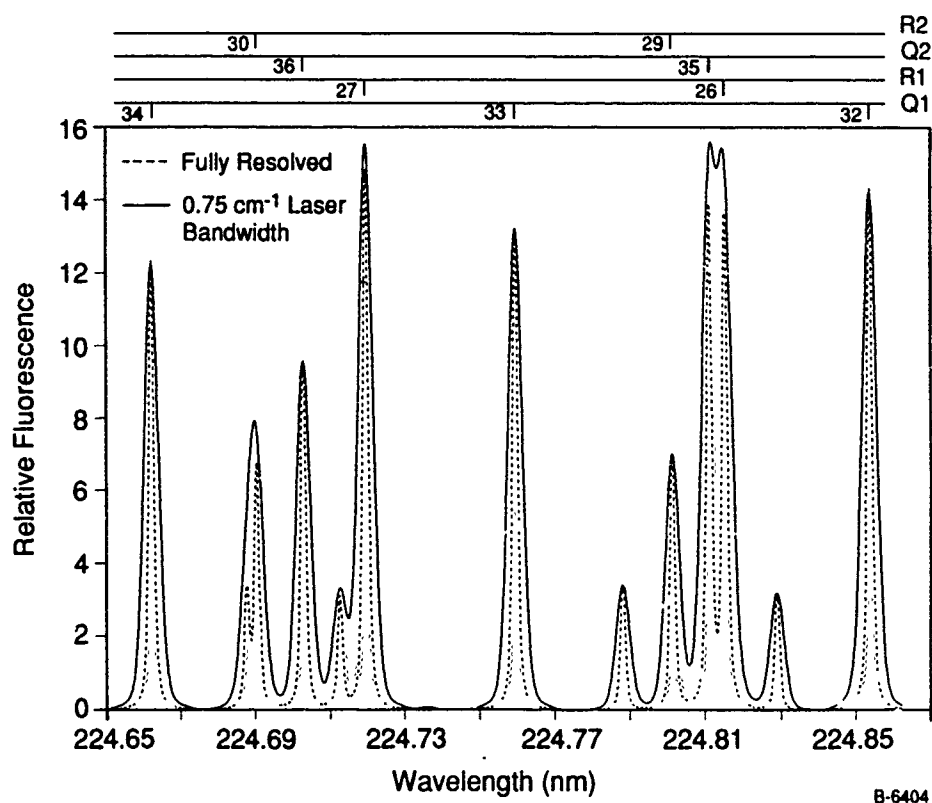


Figure 15. NO Excitation Scan Detail - 1500 K



### 4.3 Velocity Algorithm Sensitivity Analysis

The form of the velocity algorithm derived in Subsection 4.1 is an implicit relationship between the flow velocity (the desired experimental parameter) and sum/difference ratios of lineshape overlap integrals (the measured quantities). Because the expression is implicit, it is not possible to derive closed-form, algebraic expressions for the uncertainty in the inferred velocity as a function of the variation in the parameters of the overlap integrals. Nor is it possible to invert Eq. (28) so that a closed form expression for the velocity uncertainty introduced by signal uncertainty is obtained.

Instead, we have broken the problem down into two components. In Subsection 4.3.1, we examine the variation in the inferred velocity with variations in flow temperature, pressure, and laser bandwidth by calculating the velocity algorithm for a range of parameter values. When plotted together, the range of velocities which give rise to the same value of the algorithm then corresponds to the velocity uncertainty introduced by the given parameter variation.

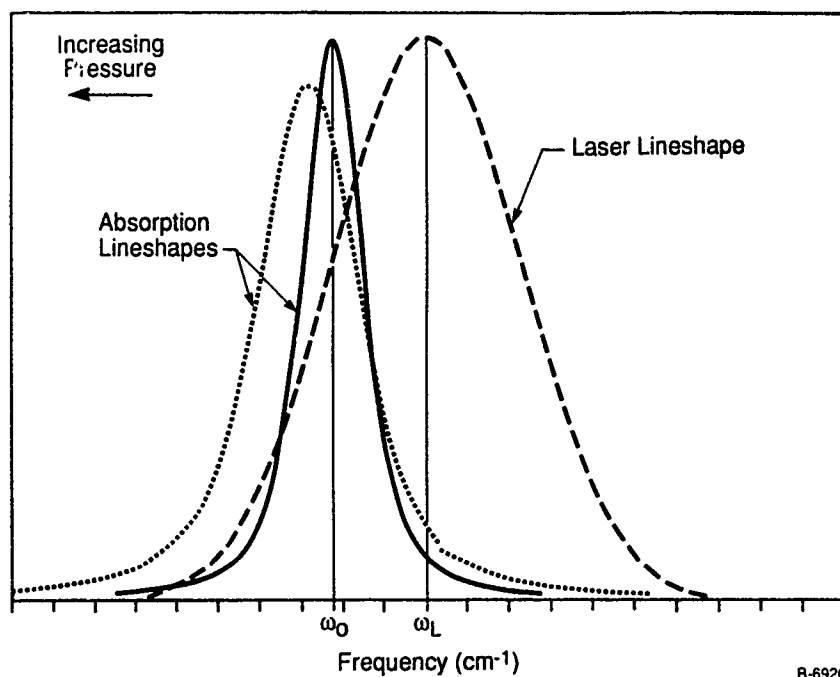
In Subsection 4.3.2, the uncertainty due to signal noise is examined explicitly. In PLIF fluorescence measurements, signal noise is almost always dominated by photon shot-noise carried on the signal itself. Because the signal level varies with the Doppler-shift (and thus the velocity) the signal/noise ratio will vary continuously with velocity. A closed form for the uncertainty in the velocity algorithm due to the signal uncertainty is derived. The velocity algorithm is then plotted against velocity with a range of algorithm values determined by the rms standard deviation due to the signal-noise. As in the previous section, this plot is examined in order to determine the range of velocities which give rise to a given value of the velocity algorithm. When the spread in the velocity algorithm due to shot noise is combined with variations in the parameters of Subsection 4.3.1, a complete map of the velocity uncertainty to signal noise and property variations is obtained.

#### 4.3.1 Variations due to Temperature, Pressure, and Laser Bandwidth

A computer routine was constructed which calculates the velocity algorithm of Eq. (28) for Voigt lineshapes and Gaussian laser spectral bandwidths as a function of the gas flow velocity. The parameters of the implicit velocity equation are the flow temperature and pressure (used to calculate the Voigt profile for the given  $a$ -parameter dependence), the laser bandwidth, and the detuning between the laser line-center and the absorption line-center at zero velocity (hereafter referred to as the static detuning). The latter parameter is the most easily controlled in the experimental design, since the laser line-center can be positioned accurately to within a small fraction of the line-width. The goal of the first phase of the modelling effort was to search for static-detunings which would result in minimum sensitivity of the velocity algorithm to changes in flow temperature and pressure over a given velocity range.

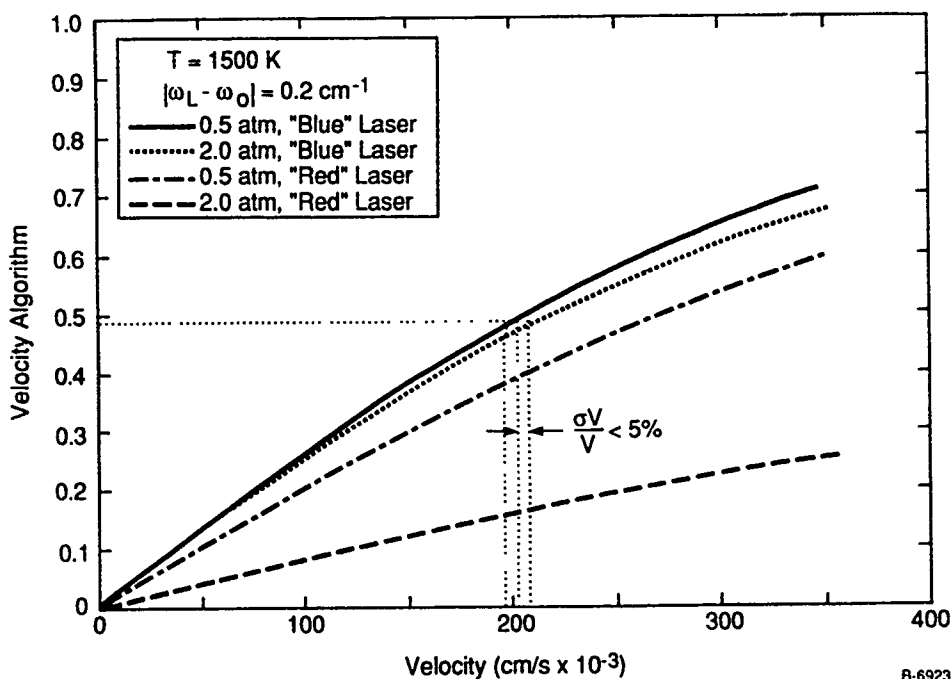
A conceptual outline of the calculation is illustrated in Figure 16, which shows the relative lineshapes of the  $0.75 \text{ cm}^{-1}$  Gaussian laser line centered at  $\omega_L$  and the NO Voigt absorption line centered at  $\omega_0$ . A second absorption lineshape is also shown, illustrating the effect of increasing pressure in broadening the absorption lineshape and shifting it to lower frequency. The pressure shift breaks the frequency domain symmetry of Eq. (28) and results in dramatically different behavior of the velocity algorithm's sensitivity to pressure depending upon whether the laser static detuning is to higher frequencies (as shown in the figure) or to lower frequencies.

Figure 17 shows the magnitude of the velocity algorithm plotted as a function of relative flow velocity for the case of 1500 K air. The curves constitute a lookup table for the velocimeter with the abscissa being the experimentally measured parameter and the ordinate being the inferred velocity. Two pressure cases are plotted, 0.5 and 2.0 atm, along with two static detunings. The top two curves show the optimum static detuning of  $\omega_L - \omega_0 = 0.2 \text{ cm}^{-1}$ , where over the full dynamic range of 3.5 km/s, the factor of four variation in pressure (a typical range for near atmospheric compressible flows) results in less



B-6920

Figure 16. Conceptual Outline of the Effect of Pressure on the Velocity Doppler-shifted Overlap of the Laser Lineshape and Absorption Lineshape



B-6923

Figure 17. Velocity Algorithm for Various Pressures

than 5 percent uncertainty in the inferred velocity. Here and throughout this report, the velocity uncertainty is defined as the half-width of the range of velocities giving rise to the same value of the velocity algorithm. Also, the velocity calculation is terminated at 3.5 km/s. At this point, the smallest signal,  $S_{F-}$ , has fallen to about 2 percent of its peak value. Hence, this large velocity dynamic range requires only a 50-1 signal dynamic range, within the linear range of intensified CCD detector systems. For the symmetric, but opposite detuning, case of a static detuning =  $-0.2 \text{ cm}^{-1}$ , i.e., the laser is tuned the same amount to the lower frequency side of the the absorption lineshape, a much different situation obtains and the measurement would be essentially meaningless in the presence of these pressure fluctuations. The reason for this asymmetry, of course, lies in the action of the collisional shifting and broadening on the absorption lineshape.

With the "blue" detuning (laser line-center at a higher frequency than the absorption line-center), as shown in Figure 15, the tendency of the collisional shift to move the value of the algorithm at any velocity further out on the convolution lineshape is balanced by the overall broadening of the lineshape so that the apparent value of the algorithm as a fraction of the broadening linewidth is changed little. In the opposite case, for the "red" detuning, the collisional shift tends to enhance the broadening of the convolution lineshape by moving the value of the algorithm nearer to the line-center of the convolution profile. As shown in Figure 7, the center of the convolution profile is less sensitive to velocity (lower values of the algorithm for every velocity) and more sensitive to pressure (larger changes in the algorithm value with pressure at a given velocity). It should be possible to find a "red" static detuning value which results in lower pressure sensitivity, but this value would lie much further out on the convolution profile so that the pressure shifts back toward line-center approach the region of maximum slope of the convolution lineshape. In this scheme, all of the fluorescence signal would be much weaker due to the reduced overlap in the wings of the convolution lineshape and the uncertainty in velocity would be much higher due to signal noise considerations, as well be discussed in the following section.

It is important to note that in Figure 17, and in all following Figures relating to the velocity algorithm, the velocity range shown is a relative range about any reference velocity. It simply refers to the velocity of the gas relative to the condition of the "static" detuning. This might often be zero velocity, but the laser wavelength could easily be tuned to correspond to the optimum detuning for gases flowing at any velocity. The magnitude of the velocity algorithm would then be used to measure velocity relative to this reference condition. As is evident in Figure 17 and in the Figures to follow, the velocity uncertainty with respect to parametric fluctuations tends to increase (as a percent of the measured value) with increasing dynamic range. Dynamic range is here defined as the range of velocities plotted, which would correspond to the range of velocities which could be imaged in a single laser pulse.

The dependence of the velocity algorithm on temperature variations is shown in Figure 18. The calculations span the range between 1000 and 2000 K at a fixed flow pressure of 1 atm. As mentioned in previous sections, the temperature dependence of the

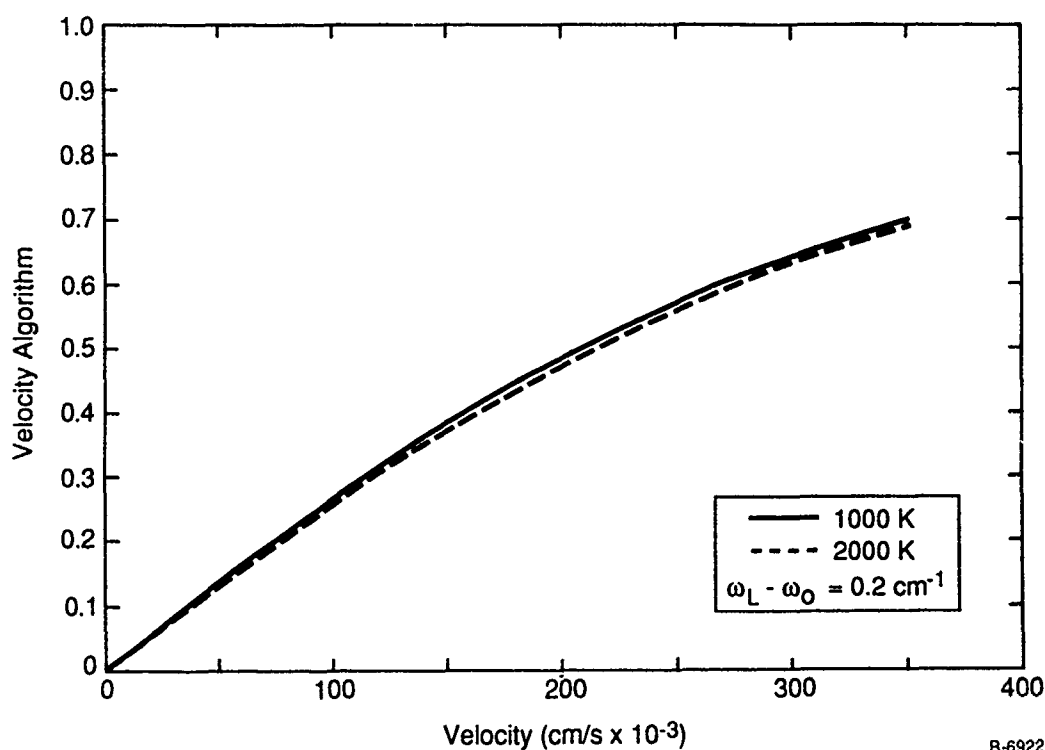


Figure 18. Velocity Algorithm for Various Temperatures

NO absorption lineshape is small, with the increased broadening of the Doppler component balanced by the decrease in the collisional component. The uncertainty in the inferred velocity is less than 2 percent over the entire range.

In a compressible flowfield, the gas pressure and temperature can not vary arbitrarily. Coupled variations may be derived by considering pressure and temperature ratios across shocks, combustion-generated heat release, or isentropic flow variations due to cross-sectional area changes or turbulence. We examined the latter case explicitly. Taking the nominal condition to be 1 atm, 1500 K, and Mach 2 (corresponding to a velocity of 134,000 cm/s), we permitted the gas flow to undergo an isentropic compression to 2 atm, 1826 K, Mach 1.54 (velocity = 114,000 cm/s) and an isentropic expansion to 0.5 atm, 640 K, Mach 2.44 (velocity = 121,000 cm/s). The velocity algorithm was calculated for each of the three conditions and the results are plotted in Figure 19 for the nominal static detuning of  $0.2 \text{ cm}^{-1}$ .

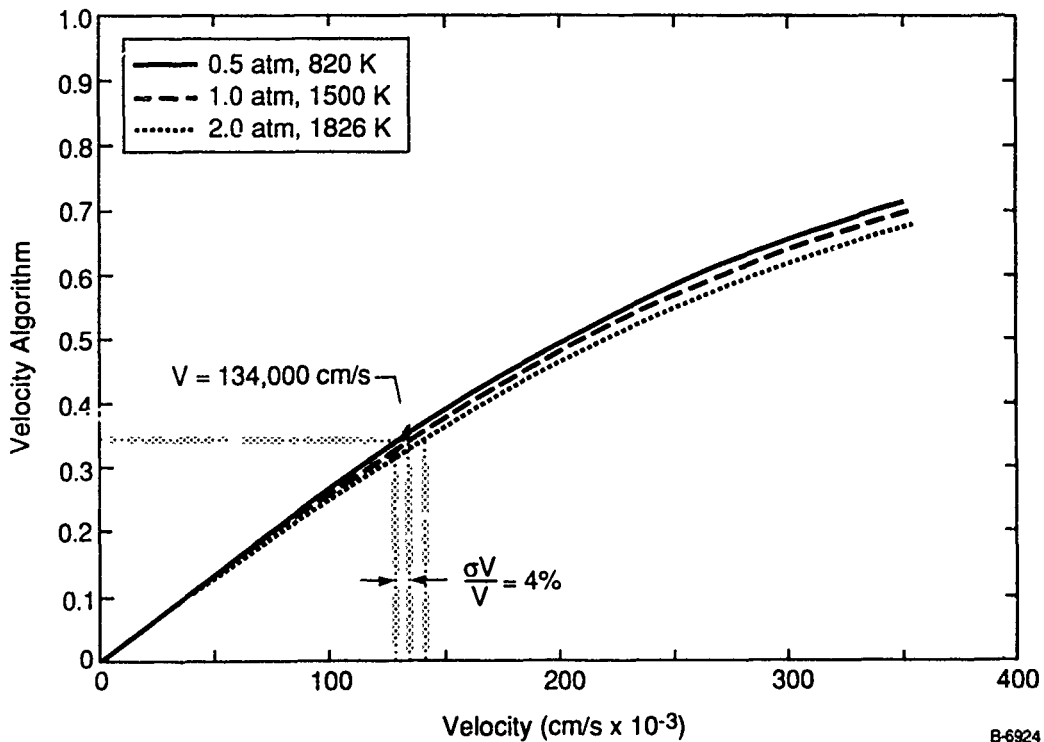


Figure 19. Velocity Algorithm for Isentropic Flow Variations

This figure shows that the competing effects of pressure and temperature balance one another so that the spread in the velocity algorithm is less than in Figure 17 for the same range of pressures. For the given flow conditions, the velocity varies by 8 percent (expansion) and 15 percent (compression), while the uncertainty at the nominal condition due to the temperature and pressure variations is only 4 percent. Hence, the uncertainty introduced in the inferred velocity is substantially less than the actual flow velocity changes. Assuming that free-stream turbulent fluctuations could be modelled as isentropic, this suggests that the velocimeter will be capable of making fluctuating velocity measurements if the velocity fluctuations are greater than about 5 percent.

The final parametric variation we consider in this section is the effect of fluctuating laser spectral bandwidths. While the mean bandwidth and profile may be accurately established, there will be some residual fluctuations in the laser bandwidth from shot to shot. These fluctuations are not well characterized by the manufacturer and we are aware of no published data on the bandwidth stability of frequency-doubled pulsed dye lasers. As a means of assessing the impact of such variations, we calculated the velocity algorithm for  $\pm 5$  percent variations in the nominal laser bandwidth of  $0.75 \text{ cm}^{-1}$ . These results are plotted in Figure 20. The velocity uncertainty at 300,000 cm/s is nearly 10 percent, the largest of the parametric uncertainties investigated. This is due to the large contribution to the convolution lineshape from the laser bandwidth.

The 5 percent bandwidth fluctuations used in this sample calculation are larger than would be expected for a typical pulsed dye laser, so we may view this uncertainty as a worst-case estimate. This source of uncertainty, however, can be removed by measuring the instantaneous bandwidth of the laser simultaneously with each PLIF measurement and using the instantaneous bandwidth in the data reduction procedure. The bandwidth of the visible laser light is measured with a fixed-spacing etalon and the fringe pattern is recorded using an unintensified linear diode array. The UV bandwidth can be calculated by multiplying the visible bandwidth by itself. In the Phase II portion of the program, this procedure for determining the bandwidth of the frequency-doubled dye laser will be verified by measuring

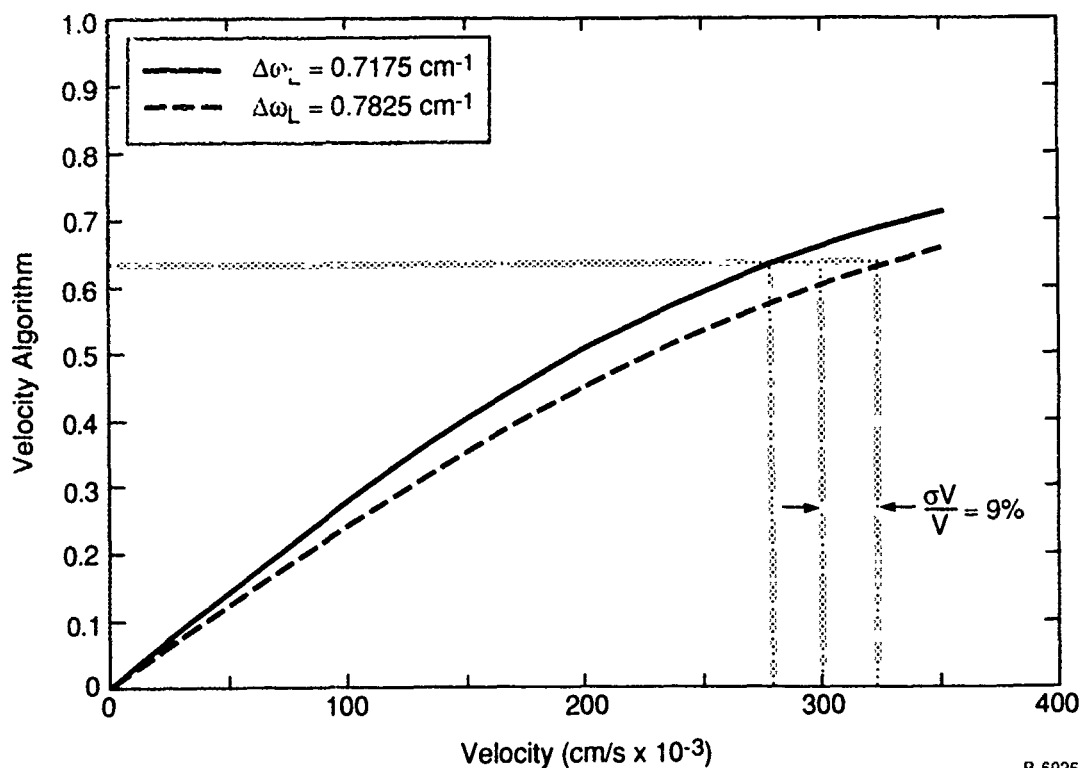


Figure 20. Velocity Algorithm for Fluctuating Laser Bandwidth

both the visible bandwidth, as described above, and the UV bandwidth using a Fabry-Perot inteferometer and intensified camera system. We have performed similar measurements on a Nd:YAG-pumped dye lasers. With this approach, the uncertainty displayed in Figure 20 may be reduced or removed completely.

The results of this systematic study of the effect of temperature, pressure, and laser bandwidth on the instantaneous velocity algorithm suggest that the most important effect is the laser bandwidth. As a consequence, the Phase II instrument would include a means of shot to shot measurement of the laser bandwidth. The following section considers the effect of signal noise.



#### 4.3.2 Signal Noise Considerations.

Recall the equation for the velocity algorithm

$$\psi(v) = \frac{S_{F^+} - S_{F^-}}{S_{F^+} + S_{F^-}} \quad (29)$$

Algebraically, this equation may be manipulated into the following form:

$$\psi(v) = \frac{2S_{F^+}}{S_{F^+} + S_{F^-}} - 1 = \frac{2S_{F^+}}{S_{F\pm}} - 1 \quad (30)$$

where  $S_{F\pm} = S_{F^+} + S_{F^-}$ . For a PLIF experiment, this form is preferred since one camera would measure only  $S_{F^+}$  while the second camera would integrate both  $S_{F^+}$  and  $S_{F^-}$ . The advantage of this is obvious if one considers that the signal noise,  $\sigma S_F$ , will be dominated by signal shot-noise which is given by

$$\sigma S_F = (\eta S_F)^{1/2} \quad (31)$$

where  $\eta$  is the detector quantum efficiency. Hence the signal-to-noise ratio is

$$\frac{S_F}{\sigma S_F} = (\eta S_F)^{1/2} \quad (32)$$

Thus integrating both  $S_{F^+}$  and  $S_{F^-}$  on the same detector avoids the low signal to noise ratio inherent in the  $S_{F^-}$  image alone.

From error propagation theory, the uncertainty in the velocity algorithm is related to the uncertainty in the measured quantities according to the equation

$$\sigma\psi^2 = \left[ \frac{\partial\psi}{\partial S_{F^+}} \right]^2 \sigma S_F^2 + \left[ \frac{\partial\psi}{\partial S_{F\pm}} \right]^2 \sigma S_{F\pm}^2 \quad (33)$$

Performing the substitution for the partial derivatives and manipulating the result algebraically, we have

$$\frac{\sigma\psi}{\psi} = \frac{2}{S_{F\pm}(2S_{F+} - S_{F\pm})} \left\{ (S_{F\pm} \sigma S_{F+})^2 + (S_{F+} \sigma S_{F\pm}^2) \right\}^{1/2} . \quad (34)$$

The actual detected signal is the number of incident photons,  $S_F$ , multiplied by the detector quantum efficiency,  $\eta$ . Substituting this and the expression in Eq. (32) for the shot-noise limited uncertainty in each signal, we have the following equation for the velocity algorithm uncertainty due to the signal uncertainty:

$$\frac{\sigma\psi}{\psi} = \frac{2}{(2S_{F+} - S_{F\pm})} \left\{ \frac{S_{F+}}{S_{F\pm}} \left[ \frac{S_{F\pm} + S_{F+}}{\eta} \right] \right\}^{1/2} . \quad (35)$$

Equation (35) shows that the fractional uncertainty in the algorithm approaches infinity as  $S_{F\pm} \rightarrow 2S_{F+}$ , or as the velocity approaches zero. The increased fractional uncertainty here is due to the problem in measuring small differences between large numbers in the presence of statistical noise.

To ascertain the impact of this additional source of uncertainty on the inferred velocity, further simulations of the velocity algorithm as a function of velocity and with the parameteric variations discussed above were undertaken. Signal levels were predicted from the formula introduced in Eq. (1).

Calculations of expected signal levels were made assuming a 5 cm x 6.7 cm imaged region, 5 percent NO in air at 1500 K and 1 atm, and typical values for the remaining parameters taken from our prior experience with NO PLIF imaging using frequency-doubled excimer-pumped dye laser excitation (cf., Ref. 23). It immediately became apparent that the signal uncertainty overwhelmed the sources of uncertainty described in the previous section by a large measure. In order to achieve reasonable uncertainty levels with realistic parameters of Eq. (1) it would be necessary to average neighboring pixels on the detector array. This decreases signal uncertainty at the expense of spatial resolution.

Figure 21 is a calculation of the velocity algorithm spread for  $\pm$  half the variation of Eq. (28) when the detector pixels are averaged in blocks of 10. For the intensified CCD arrays available at PSI, with 512 x 240 elements, this would correspond to an effective resolution of  $\sim 100 \times 100$ . This lower resolution is still useful, representing over 10,000 individual measurement locations in every laser shot. With this averaging, the instantaneous velocity uncertainty due to the signal noise is less than 5 percent at 2 km/s.

A similar calculation for the isentropic flow variations of the previous section is shown in Figure 22. Here, the instantaneous velocity uncertainty is on the order of 10 percent, as opposed to 4 percent in the earlier calculation. Hence, it may not be possible to *image* free-stream turbulent fluctuations because of the inherently low signal levels associated with imaging experiments. The uncertainties of Figure 21 could be achieved in point measurements, however, where the signal levels are much higher due to high laser intensities (concentrating the available laser energy into a single collection volume) and larger optical collection efficiencies. Lower uncertainties in *mean* velocity distributions may be

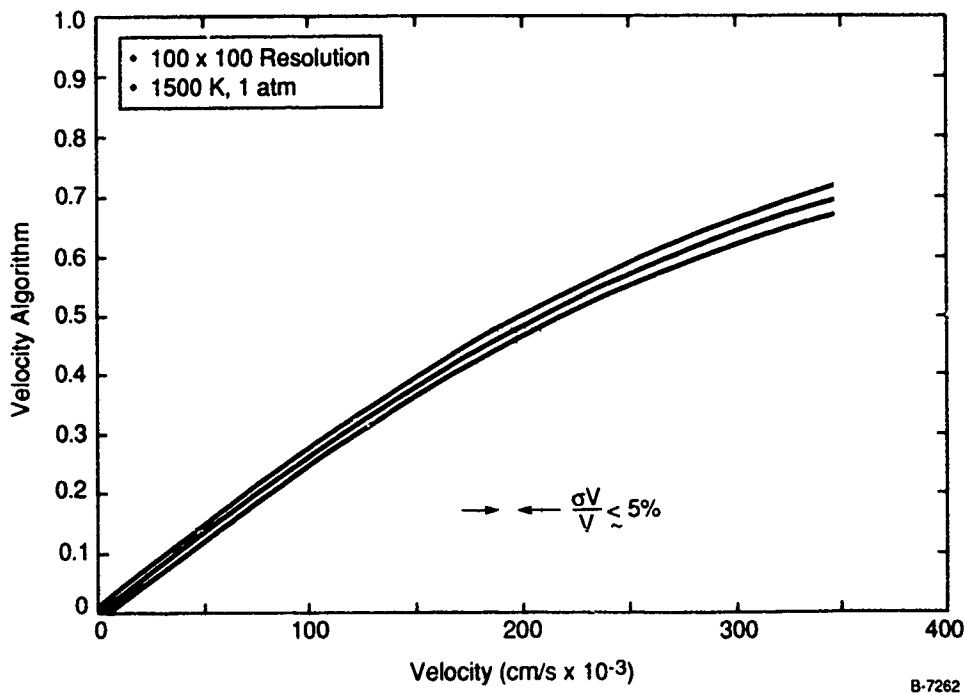


Figure 21. Velocity Algorithm for Shot-Noise Limited Signals

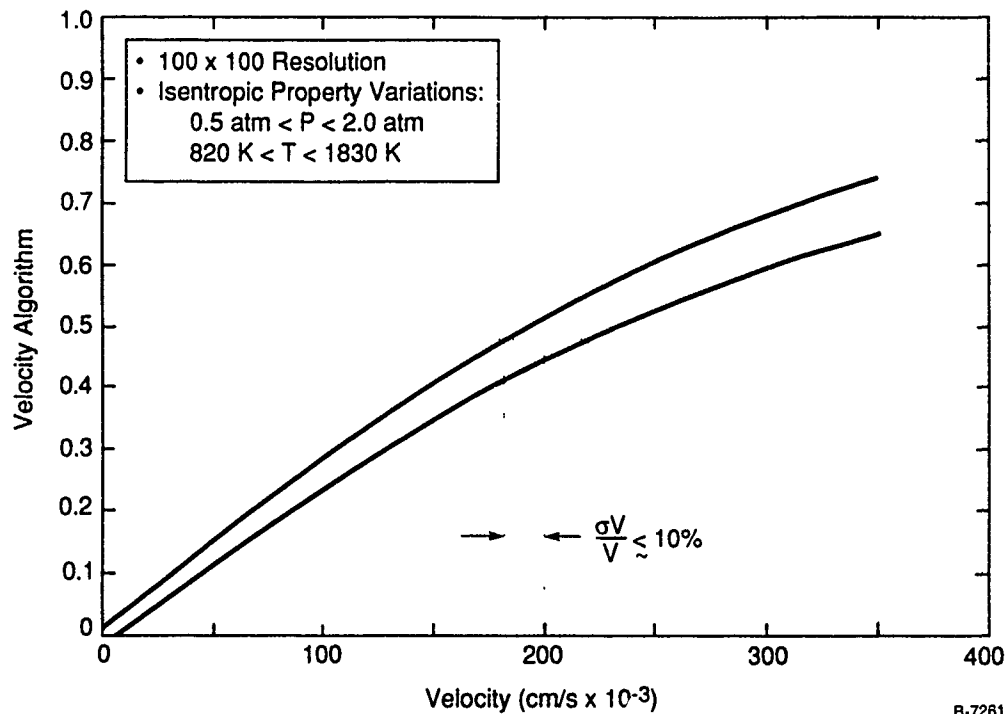


Figure 22. Velocity Algorithm for Isentropic Flow Variations in the Presence of Signal Shot-Noise

achieved in imaging measurements by averaging multiple velocity images together. For example, averaging 10 velocity images, obtained approximately 1s apart with the current PSI imaging systems, would result in a noise reduction of approximately 3, which is the residual uncertainty associated with the isentropic variations, which averaging will not remove.

In summary, this section has detailed the sensitivity of the proposed velocimeter to unmeasured variations in the flowfield properties, laser spectral properties, and signal noise. Laser spectral bandwidth fluctuations were shown to be the largest parameteric source of velocity uncertainty due the large contribution of the laser spectral bandwidth to the convolution lineshape. This source of uncertainty may be removed by monitoring the instantaneous laser bandwidth with a second detector arm, as described. A signal shot-noise analysis was presented for typical NO PLIF imaging configurations and the contributions of the shot-noise to the velocity uncertainty derived. By averaging together groups of

5 x 2 pixel sub-arrays, resulting in an overall array dimension of 102 x 120, the shot-noise contribution to the velocity uncertainty at the reference conditions of 1500 K and 1 atm was reduced to approximately 5 percent. Using this reduced resolution array approach, it was shown that isentropic compressions and expansions covering a factor of 4 in pressure around the reference condition and including the shot-noise variations resulted in instantaneous velocity uncertainties on the order of 10 percent.

## 5. DEVELOPMENT OF HIGH PRESSURE, SUPERSONIC BURNER

This section describes a significant engineering development task of this Phase I program. As detailed in the previous sections, the LIF velocimetry technique is sensitive to flowfield property variations. It is therefore critical that the technique be quantitatively examined at flow temperatures and pressures of interest in the final application. For the purposes of this program, these conditions are representative of supersonic propulsion facilities: approximately  $1000\text{ K} < T < 2000\text{ K}$ ,  $0.5 < P < 2\text{ atm}$ , and  $3 \times 10^4\text{ cm/s} < v < 3 \times 10^5\text{ cm/s}$ . Furthermore, the flowfield within the facility may include large pressure and temperature variations due to shock waves and combustion-generated heat release. A velocity imaging technique should be insensitive to these property variations since simultaneous measurements may not be available.

Our goal in this portion of the Phase I program was to develop a laboratory-scale, stable source of high velocity NO at these conditions. The source should have an adjustable range of NO number density, flow temperature, velocity, and pressure. Furthermore, since detailed PLIF measurements are envisioned, the flow should be large enough for the imaging technique to resolve spatial variations and to permit comparison to scanned pulsed-dye laser measurements at multiple single-point flowfield locations. Finally, the flowfield should be amenable to analytical determination of the property variations so that the experimental data may be compared to theoretical predictions.

### 5.1 Burner Overview

Our approach for this problem was to develop a high-pressure hydrogen-air burner. The choice of hydrogen combustion is driven by the desire to generate the highest possible plenum temperatures as well as to approximately match NASP-type SCRAMjet chemical flowfields. The high-temperature exhaust products from this burner can be accelerated through a round orifice into the atmosphere, creating an underexpanded round jet. This type of flowfield has been well studied (cf., Refs. 24 and 25) so that our measurements may be

compared to other experimental and analytical studies. For burner design pressures up to 100 psi, the exit pressure ratio of 6.8 will generate flow velocities up to  $1 \times 10^5$  cm/s. The hot exhaust gases will contain some concentrations of NO, depending on the gas temperature that is obtained within the burner. The NO density may be independently adjusted by added small quantities (nominally a few percent by volume) to the plenum flow.

A schematic diagram of the burner is shown in Figure 23. The body of the burner consists of a 4 in. I.D. copper cylinder. The nozzle was machined from bronze, providing a compromise between high thermal conductivity and good machining properties. The exhaust exit diameter is 0.5 cm. The primary fuel and air injection is provided through the bronze baseplate of the burner. The main injector is an annulus consisting of a 1 in. stainless steel

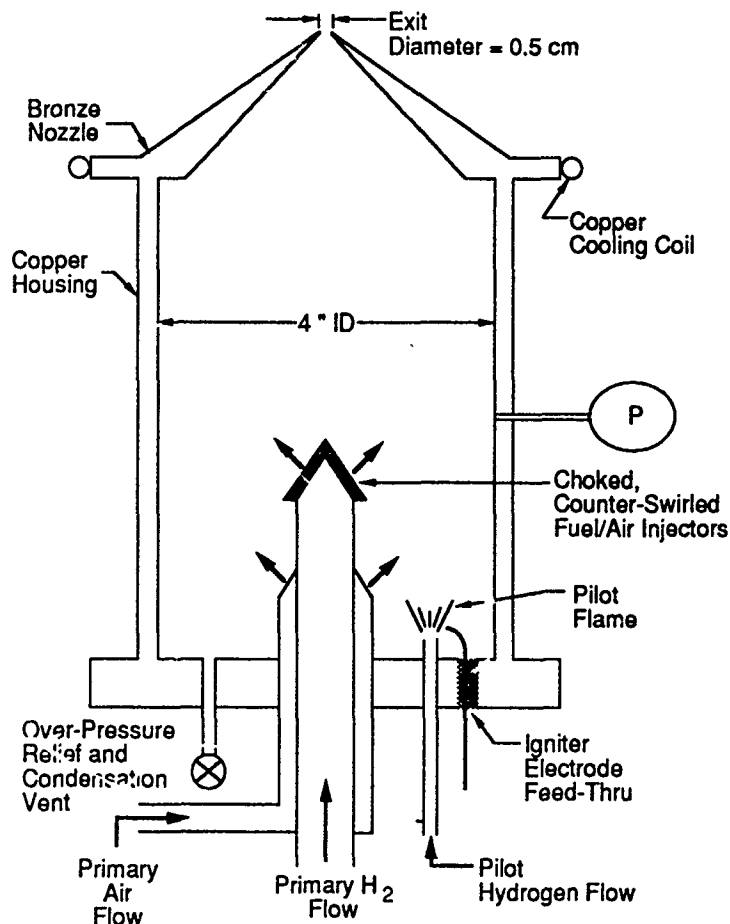


Figure 23. Schematic of High-Pressure Hydrogen-Air Burner

outer tube flowing hydrogen with a 5/8 in. inner tube for the air. The primary flow is continuously ignited with a small, 1/4 in. pilot flow of hydrogen. The pilot flame is ignited at the beginning of an experiment with a spark electrode fitted through the burner baseplate.

Condensation of the water vapor at the burner walls is vented through a 1/4 in. valve, also located in the baseplate. This valve also contains a relief stem in the event of an over-pressure within the burner. Burner pressure is monitored with a pressure tap connected to a Bourdon-tube pressure gage. The gas velocities are controlled and metered with a rotameter panel. Flow delivery pressures are also monitored. The primary hydrogen flow passes through an electronic shut-off valve which is controlled by the burner pressure. If the pressure suddenly drops below the operating condition (i.e., an explosive failure) the hydrogen flow is automatically shut-off. A thermocouple is used to monitor the temperature of the nozzle/burner O-ring seal, which can be safely operated up to about 200°C.

A schematic diagram of the underexpanded jet at the maximum operating pressure is shown in Figure 24 (from Ref. 16). For expansion pressure ratios of about 7 and above, the characteristic barrel shock pattern and Mach disk is observed. The flow accelerates from Mach 1 at the nozzle exit to about Mach 3.5 at the Mach disk. Radially beyond the barrel shock is a lower velocity supersonic flow. Axially beyond the Mach disk, the flow is initially subsonic, thereafter relaxing to the ambient pressure field through a series of diamond shock/expansion waves. Along the nozzle centerline the temperature and pressure drop, until the Mach disk, where they suddenly increase. Further details of this flowfield may be found in Ref. 25. Figure 18 shows that, in the space of a few nozzle diameters, the flowfield contains a variety of temperature, velocity, and pressure ranges. Hence, it is an ideal test flow for the LIF velocimetry approach.

The original injector design consisted of straight tube flow. A large velocity mismatch between the outer fuel and central air flows was planned in order to induce a high level of mixing between the two flows and, ideally, efficient and even burning. Early shake-



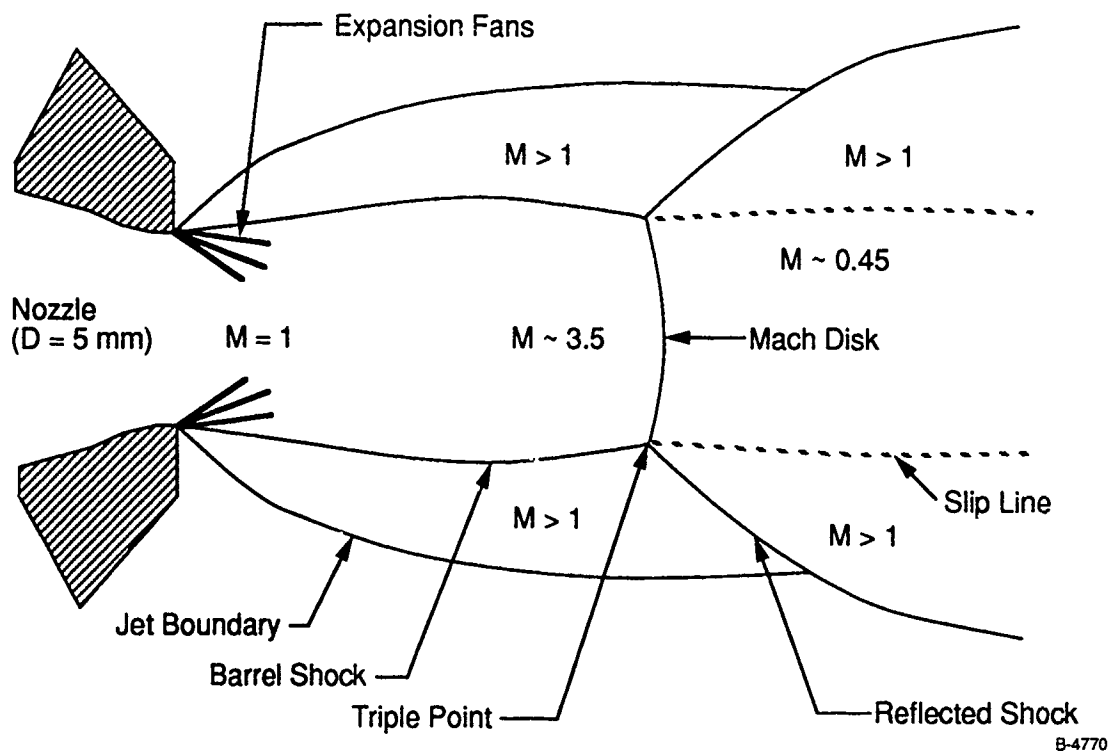


Figure 24. Schematic Diagram of Underexpanded Jet Flowfield for an Expansion Ratio  $\sim 7$

down experiments, however, proved that this was not the case. The fuel and air mixing was very poor, such that unmixed gases flowed out of the nozzle and ignited in free jet.

The primary injector was modified by capping the annular air and  $H_2$  tubes with choked, counter-swirled "shower-head" distribution covers. With this modification, mixing within the burner was much more efficient, as evidenced by a factor of  $\sim 2.5$  increase in burner pressure due to combustion. The burner was operated up to its design pressure of 100 psi. Pressure fluctuations, however, persisted at a level of approximately  $\pm 5$  psi on the pressure gage. Since the Bourdon-tube gage does not have good high frequency response, we can assume that the pressure fluctuations within the burner itself were significantly larger.

The residual fluctuations may be due to incomplete choking of the  $H_2$  injector or coupling through the un-choked pressure tap or pilot flame. We plan to modify the burner to reduce these instabilities.

During the course of the shakedown testing, the injector tube overheated, causing the silver-soldered distribution cap of the  $H_2$  tube to blow off. Unfortunately, the design of the injector was such that it could not be modified without replacing entirely. Within the financial and temporal constraints of the Phase I portion of the program, such a comprehensive modification was not feasible.

We continued to work with the flow by supplying high pressure air through both the  $H_2$  and air injector paths. In this manner, cold (room temperature plenum) air flows were generated with a maximum internal pressure of 50 psi. With this pressure ratio of approximately 3, the flowfield downstream of the orifice is substantially different from that shown in Figure 24. A schematic diagram is shown in Figure 25 (taken from Ref. 26).

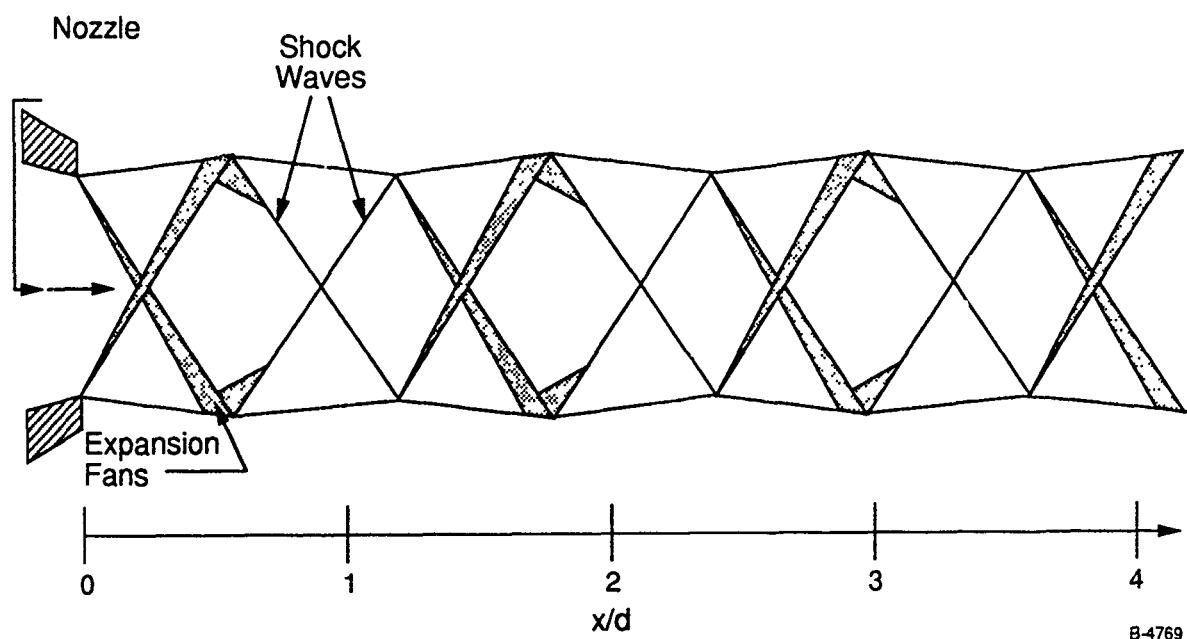


Figure 25. Schematic Diagram of Underexpanded Jet Flowfield for an Expansion Ratio  $\sim 3$

The lower expansion ratio does not produce a Mach disk or barrel shock. Instead, the flow relaxes to the back ground pressure through a series of alternating expansion fans and shock waves. The repeated pattern along the jet axis is typically referred to as the diamond shock pattern.

## 5.2 PLIF Imaging of NO Distributions in Exhaust Jet

Scanned Doppler-shifted velocity measurements in the cold supersonic flowfield of Figure 24 were not feasible due to the thermodynamic properties of this jet. Because the plenum temperature was only room temperature, the Mach 1.5 flow would cool to about 200 K and expand to  $\sim 10$  psi. At these conditions, the NO absorption linewidths are collisionally dominated and approximately  $0.6 \text{ cm}^{-1}$ . Hence, the convolution linewidth obtained by scanning the pulsed laser bandwidth over this feature would be nearly  $1 \text{ cm}^{-1}$ , whereas the maximum Doppler-shift would be on the order of  $0.03 \text{ cm}^{-1}$ . Furthermore, the pressure-dependent collisional shift is on the order of  $0.2 \text{ cm}^{-1}$ , more than six times the velocity shift. Since we had no way of accurately measuring the pressure in the jet flow, it would not be possible to distinguish the small Doppler-shift in the presence of uncertain pressure-shifts.

In order to verify the gross characteristics of the flowfield, we seeded the air-only flow with a small amount of NO and visualized the cold exhaust flow using PLIF imaging. The images were taken using the excimer-pumped tunable, pulsed dye laser and a PSI intensified CCD array camera. The laser beam was focused into a thin sheet and directed across the centerline of the jet flow. At right angles to the laser sheet, the NO fluorescence from seven laser pulses was collected and digitized. An example of such an image is shown in Figure 26. The NO fluorescence intensity is false-color encoded according to the color lookup table shown. The laser wavelength was tuned to the partially resolved  $Q_1$  ( $1 \leq N'' \leq 3$ ) bandhead at 226.257 nm. The region viewed is  $4.5 \times 3.5$  cm with the nozzle exit at the bottom. The low  $N$ 's used in the excitation process are well below the peak  $N$  levels for the jet exit temperature. Hence, the signal will increase as the gas expands

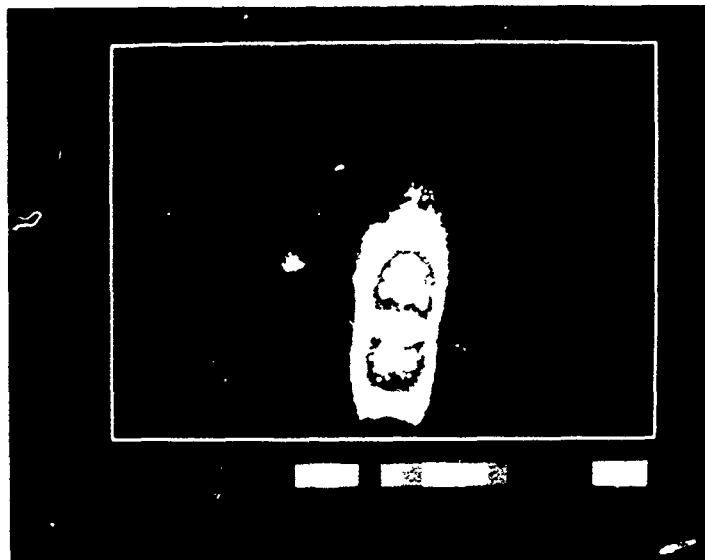


Figure 26. NO PLIF Image in Supersonic Flowfield

into colder, lower density regions and the Boltzmann population fraction shifts to lower N's. This is observed in Figure 26 as a gradually increasing signal level through the expansion fans in the first diameter downstream of the exit plane. Across the recompression shocks, the temperature suddenly increases and there is a corresponding instantaneous drop in signal level. Comparison of the distribution of fluorescence in Figure 26 with the schematic diagram of the mean flow structure in Figure 25 shows that the expected alternating diamond pattern of low and high density is present. A slight tilt of the jet is noticeable as well. The burner can was visually straight in the lab, so the flow angle may be due to a nozzle non-uniformity.

We plan to substantially modify the burner in support of another program during the coming months. The goal of the modifications is to reduce the pressure instabilities and

improve the uniformity of the exhaust flow. Among the modifications we will be investigating are increasing the number of fuel/air mixing ports or platinum catalyst-stabilized combustion. We anticipate that the burner shakedown and evaluation studies will be completed prior to the start of the Phase II portion of this program.

## 6. CONCLUSIONS AND SUMMARY

This Phase I SBIR program successfully demonstrated the feasibility of several key elements of a LIF velocimeter based on NO fluorescence. An analytical treatment of Doppler-shifted fluorescence was developed which expresses the various approaches for velocity measurements in a unified context. Using this derivation, a detailed model of the Doppler-shifted fluorescence approach necessary for single-shot velocity imaging was constructed. An extensive modelling study showed that a single broadband, pulsed dye laser can obtain time-resolved velocity measurements without an in-situ, simultaneous measurement of temperature or pressure. Pressure variations from 0.5 to 2 atm were shown to have a less than 10 percent effect on the velocity inferred from the fluorescence signal. Temperature variations from 1000 to 2000 K had a negligible impact on the inferred velocity.

A full simulation of the proposed imaging velocimeter was carried out for typical isentropic flow property variations about a nominal Mach 2, 1500 K, atmospheric pressure air flow. The simulation calculated the expected signal levels based on realistic imaging configurations, available laser power, and known spectroscopic data so that signal shot-noise effects could be included in the accuracy analysis. For flows where the pressure and temperature field were known, the single-shot velocity uncertainty over a 3.5 km/s dynamic range was less than 5 percent. For isentropic flow variations over a factor of four pressure variation, the single-shot uncertainty was on the order of 10 percent. These accuracies were for an instantaneous imaging resolution of  $\sim 100 \times 100$  pixels over a 5 cm field of view.

Our single laser approach greatly simplifies the hardware necessary to carry out a velocity measurement. The simplified setup increases the number of available users of the velocimetry technique since single laser systems are more commonly found in test facility installations. Of course, additional lasers may be integrated with the single laser approach described here in order to simultaneously measure temperature and pressure. In many flows, however, the additional complexity and optical access required for these approaches may not be feasible.

Several key experimental results were also obtained. A novel frequency-doubled ring-dye laser was operated single longitudinal mode at wavelengths near 226 nm. Using this laser, fully resolved absorption measurements of the NO lineshape broadening parameter for collisions with  $N_2$  were obtained. This important data is required in the reduction of the Doppler-shifted fluorescence signal. Extension of this database to  $O_2$ ,  $H_2O$ , and NO collisions as a function of temperature will constitute an important part of the Phase II effort.

Also, progress was made on a high-pressure, high-temperature supersonic burner facility. Nascent NO in the high-temperature gases will be supplemented by additional NO, mixed into the burner plenum, to generate a nominally Mach 3, atmospheric pressure jet flow with a maximum temperature on the order of 1500 K. This unique facility duplicates the fluid dynamic environment of typical supersonic/hypersonic propulsion test facilities and will constitute a principle test bed for the validation studies of the Phase II portion of the program. Hydrogen/air combustion was demonstrated with a maximum burner plenum pressure of 80 psi. The burner design pressure is 100 psi. Shakedown testing was plagued with persistent combustion-driven pressure instabilities which prohibited extended hot flow testing. Initial PLIF images of the NO distribution in a  $\sim$  Mach 1.5 cold air jet near atmospheric pressure were obtained.

## 7. ACKNOWLEDGEMENTS

The authors acknowledge the assistance of Michael DiRosa and Albert Chang, graduate students in the High Temperature Gasdynamics Laboratory at Stanford University, in performing the high resolution lineshape measurements under the Stanford subcontract. Mr. Chang provided much unpublished information on the role of collisional shifting in the NO lineshapes. Jerry Seitzman, of Stanford, provided the code for predictions of the NO absorption spectra. Professor Ron Hanson, also of Stanford, supervised the Stanford subcontract and provided numerous suggestions and helpful comments on the work described in this report.

At PSI, Andy Burbo performed the machining and much of the assembly of the supersonic burner. Dr. William Marinelli was the technical reviewer and participated in many stimulating and enlightening discussions.



## 8. REFERENCES

1. Hiller, B. Booman, R.A., Hassa, C., and Hanson, R.K., "Velocity Visualization in Gas Flows Using Laser-Induced Phosphorescence of Biacetyl," *Rev. Sci. Instrum.* **55**(12), 1964 (1984).
2. Miles, R.B., Connors, J.J., Markovitz, E.C., Howard, P.J., and Roth, G.J., "Instantaneous Profiles and Turbulence Statistics of Supersonic Free Shear Layers By Raman Excitation Plus Laser-Induced Electronic Fluorescence (RELIEF) Velocity Tagging of Oxygen," *Exp. in Fluids* **8**, 17 (1989).
3. Boedeker, L.R., "Velocity Measurement By  $\text{H}_2\text{O}$  Photolysis and Laser-Induced Fluorescence of OH," *Opt. Lttrs.* **14**(10), 473 (1989).
4. Goss, L.P., Chen, T.H., Trump, D.D., Sarka, B., and Nejad, A.S., "Flow-Tagging Velocimetry Using UV-Photodissociation of Water Vapor," Paper No. 91-0355, presented at the 29th Aerospace Sciences Meeting, Reno, 1991.
5. Piper, L.G. and Cowles, L.M., "Einstein Coefficients and Transition Moment Variation for the  $\text{NO}$  ( $\text{A}^2\Sigma^+ - \text{X}^2\Pi$ ) Transition," *J. Chem. Phys.* **85**(5), 2419 (1986).
6. Timmerman, A. and Wallenstein, R., "Doppler-Free Two-Photon Excitation of Nitric Oxide with Frequency-Stabilized CW Dye Laser," *Opt. Comm.* **39**(4), 239 (1981).
7. Earls, L.T., "Intensities in  $^2\Pi - ^2\Sigma$  Transitions in Diatomic Molecules," *Phys. Rev.*, **48**, 423 (1935).
8. Measures, R.M., "Selective Excitation Spectroscopy and Some Possible Applications," *J. Appl. Phys.* **39**, 5232 (1968).
9. Zimmerman, M. and Miles, R.B., "Hypersonic-Helium-Flowfield Measurements with the Resonant Doppler Velocimeter," *Appl. Phys. Lett.* **37**, 885 (1980).
10. Chang, A.Y., Battles, B.E., and Hanson, R.K., "Simultaneous Measurements of Velocity, Temperature, and Pressure Using Rapid CW Wavelength-Modulation LIF of OH," *Opt. Lttrs.* **15**(12), 706 (1989).
11. Mitchell, A.C.G. and Zemansky, M.W., Resonance Radiation and Excited Atoms, (Cambridge University Press, 1971).
12. Rea, E.C., Jr., Chang, A.Y., and Hanson, R.K., "Collisional Broadening of the  $\text{A}^2\Sigma^+ - \text{X}^2\Pi$  (0,0) Band of OH by  $\text{H}_2\text{O}$  and  $\text{CO}_2$  in Atmospheric-Pressure Flames," *J. Quant. Spectrosc. Radiat. Transfer* **41**(1), 29 (1989).

13. Dodge, L.G., Dusek, J., and Zabielski, M.F., "Line Broadening and Oscillator Strength Measurements for the Nitric Oxide  $\gamma$  (0,0) Band," J. Quant. Spectrosc. Radiat. Transfer 24, 237 (1980).
14. DiRosa, M.D., Chang, A.Y., Davidson, D.F., and Hanson, R.K., "CW Laser Strategies for Multi-Parameter Measurements of High-Speed Flows Containing Either NO or O<sub>2</sub>," Paper No. 91-0359, AIAA 29th Aerospace Sciences Meeting, 1991.
15. Varghese, P. and Hanson, R.K., "Collisional Narrowing Effects on Spectral Lineshapes Measured at High Resolution," App. Opt. 23(14), 2376 (1984).
16. Humlicek, J., "An Efficient Method for Evaluation of the Complex Probability Function: The Voigt Function and Its Derivatives," J. Quant. Spectrosc. Radiat. Transfer 21, 309 (1979).
17. Armstrong, B.H., "Spectrum Line Profiles: The Voigt Function," J. Quant. Spectrosc. Radiat. Transfer 7, 61 (1967).
18. McDaniel, J.C., Hiller, B., and Hanson, R.K., "Simultaneous Multiple-Point Velocity Measurements Using Laser-Induced Iodine Fluorescence," Opt. Ltrs. 8(1), 51 (1983).
19. Hiller, B., McDaniel, J.C., Rea, E.C., Jr., and Hanson, R.K., "Laser-Induced Fluorescence Technique for Velocity Field Measurements in Subsonic Gas Flows," Opt. Ltrs. 8(9), 474 (1983).
20. Hiller, B. and Hanson, R.K., "Simultaneous Planar Measurements of Velocity and Pressure Fields in Gas Flows Using Laser-Induced Fluorescence," App. Opt. 27(1), 33 (1988).
21. Paul, P.H., Lee, M.P., and Hanson, R.K., "Molecular Velocity Imaging of Supersonic Flows Using Pulsed Planar Laser-Induced Fluorescence of NO," Opt. Ltrs. 14(9), 417 (1989).
22. Herzberg, G., Molecular Spectra and Molecular Structure: I. Spectra of Diatomic Molecules, 2nd edition, (Van Nostrand Reinhold Co., New York, 1950).
23. Allen, M.G., Donohue, K., and Davis, S.J., "Species and Temperature Imaging in Liquid-Fueled Spray Flames," Paper No. 90-2440, AIAA/ASME/SAE/ASEE 26th Joint Propulsion Conference, July 1990.
24. Askenas, H. and Sherman, F.S., "The Structure and Utilization of Supersonic Free Jets in Low Density Wind Tunnels," in Rarefied Gas Dynamics 2 (Academic Press, New York, 1966).

25. Ewan, B.C.R. and Moodie, K., "Structure and Velocity Measurements in Underexpanded Jets," Combust. Sci. Tech. 45(6), 275 (1986).
26. Hiller, B.H., "Combined Planar Measurements of Velocity and Pressure in Compressible Gas Flows Using Laser-Induced Iodine Fluorescence," Topical Report T-256, Department of Mechanical Engineering, Stanford University, 1986.

## ADDENDUM

### Doppler-Shifted NO Fluorescence Measurement

The following section describes a proof-of-concept experiment completed under the Phase I program after the submission deadline of the Phase I Final Report. The results were included in the Phase II proposal and are described in more detail here.

#### A.1 Introduction

The body of the Phase I final report analyzes in detail the importance of an accurate description of the NO absorption/fluorescence lineshape in Doppler-shifted fluorescence velocimetry. In particular, the various roles of pressure and temperature in determining the width and line-center of a static (zero-velocity) profile were discussed. The experiment described in this addendum was undertaken to demonstrate that, in a strongly compressible flowfield, a Doppler-shifted NO fluorescence lineshape could be measured. Further, the measured lineshape could be used to infer the local gas velocity in the presence of competing collisional and thermal broadening and shifting mechanisms. While the Phase II program will focus on instantaneous *imaging* measurements, calculation of the gas velocity from the NO PLIF images will require an analytical description of the NO lineshape which is demonstrated in this result. A technique similar to that demonstrate here will be used in the Phase II program to obtain the baseline velocity profiles for comparison with the velocity imaging results.

#### A.2 Experimental Description and Results

The goal of this experiment was to fully resolve an isolated NO fluorescence lineshape in a compressible flow using the high spectral resolution ring-dye laser described in Section 3 of the Final Report. The lineshape from the flowfield was compared to a lineshape recorded simultaneously in a static cell. The frequency shift between the two lineshapes, due to both the velocity-dependent Doppler effect and collisional shifting, was analyzed to yield the mean flow velocity at a point in the flowfield.

A schematic diagram of the experimental setup is shown in Figure A.1. The output from the frequency-doubled ring-dye laser was tuned near the  $Q_2(7)$  transition at 226.72 nm and split into two beam paths. One path was directed through a static cell filled with a mixture of a fraction of a percent of NO and a few torr of  $N_2$ . This beam path was used to record the fully resolved absorption lineshape as the laser wavelength was scanned. The second beam path was focussed at the centerline of a supersonic jet approximately 1 diameter downstream of the jet orifice. The laser beam was propagated at 60 degrees with respect to the flow axis to provide a non-zero scalar product of the gas velocity and laser beam wave vector. Fluorescence from the focal volume ( $\sim 1 \text{ mm}^3$ ) was collected using a spectrally

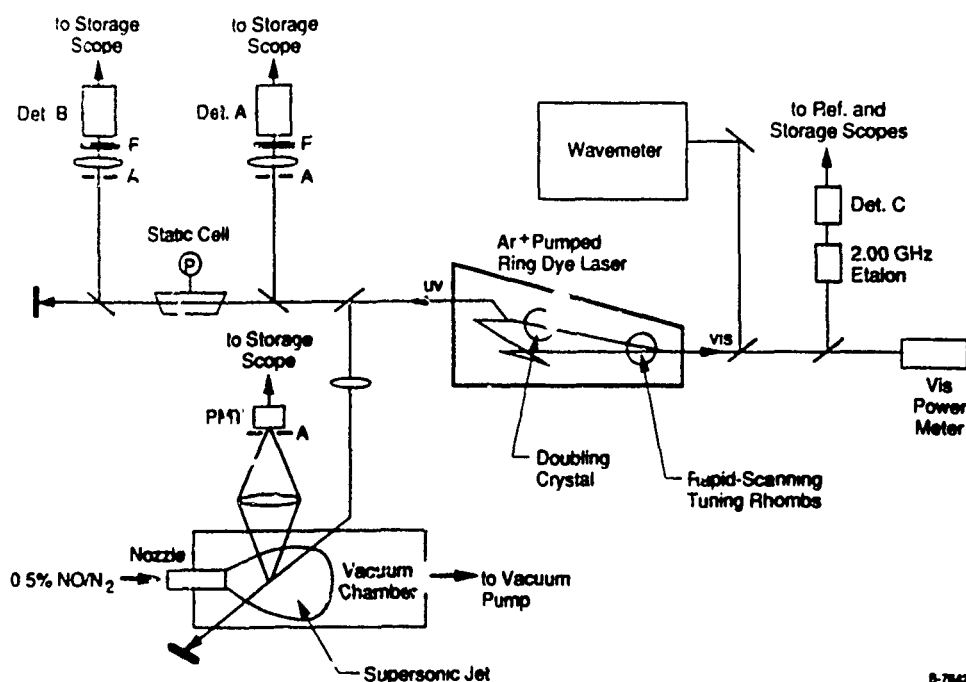


Figure A.1 Experimental Setup for Doppler-Shifted Velocity Measurement

filtered photomultiplier tube. As the laser wavelength was scanned, this beam path generated a Doppler-shifted lineshape for comparison to the static cell lineshape.

The jet reservoir was an atmospheric pressure, 300 K plenum of  $N_2$  which was seeded with 0.5 percent NO. The gas mixture expanded through the converging nozzle and emerged into the 10 torr background chamber as an underexpanded jet. The facility was exhausted through a vacuum pump in order to maintain the 10 torr background. At the measurement location, the gas temperature is approximately 70 K and the Mach number approximately 4 (cf., Ref. 11 from the Phase I Final Report).

An example data set is shown in Figure A.2. The dashed line is the *absorption* profile recorded across the static cell. The solid line is the *fluorescence* profile recorded simultaneously from the jet. The fluorescence profile is shifted with respect to the absorption profile by - 2.04 GHz. Using the flow temperature estimate, the fluorescence lineshape was fitted to a Voigt profile to extract the local flow pressure. The best Voigt fit corresponded to a flow pressure of 35 torr. From Eqs. (12) and (13) of the Final Report, the collisional shift at these conditions was calculated to be -0.6 GHz. The remaining -1.44 GHz shift is due to the component of the gas velocity vector aligned with the laser beam propagation axis. From Eq. (2), this velocity component is 33,000 cm/s, corresponding to a directed axial component of 66,000 cm/s. At ~ 70 K, this corresponds to a flow Mach number of 3.9, in good agreement with the expected value.

This experiment demonstrates several key features important to the proposed Phase II program. Firstly, and most importantly, it demonstrates that the models developed in the

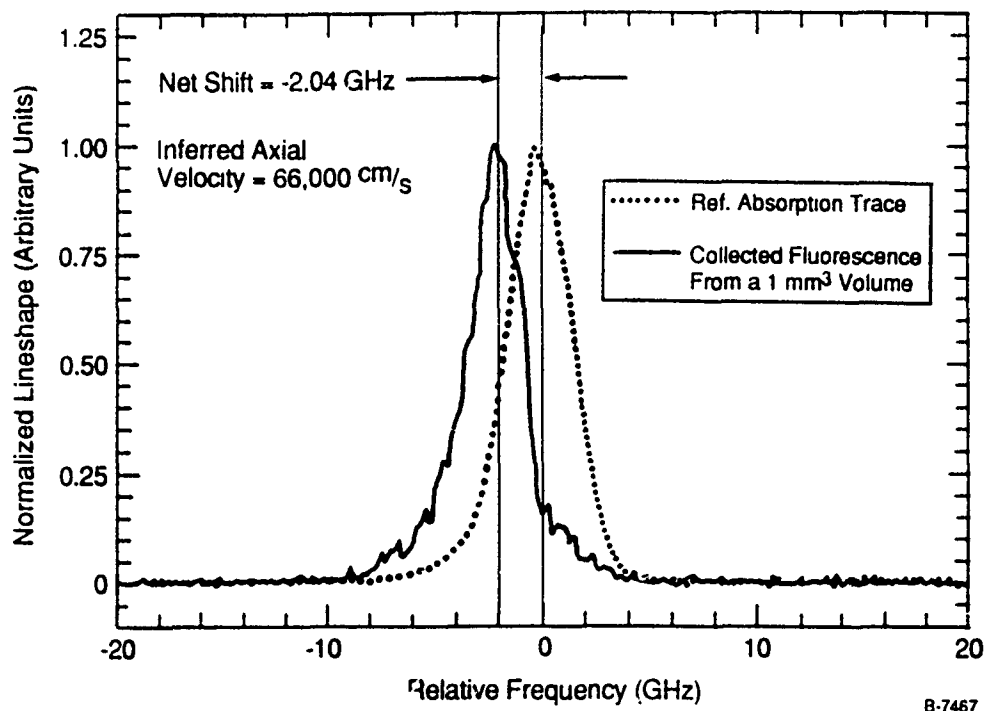


Figure A.2 Comparison of NO  $Q_2(7)$  Absorption and Fluorescence Lineshapes Acquired in a Static Cell and Supersonic Jet, Respectively.

Phase I program to describe the NO lineshape are accurate. Extracting velocity from Doppler-shifted profiles in this manner is critically dependent upon understanding of Doppler- and pressure-shifting as well as Voigt-broadening. The measured shift was slightly more than the FWHM of the fluorescence lineshape, but nearly 30 percent was due to the pressure difference between the flow and reference cell. Without accurate knowledge of the  $N_2$  broadening and shifting parameters, it would not have been possible to determine the correct flow velocity.

Secondly, this experiment demonstrated the principle of the measurements which will be used to characterize the baseline velocity, temperature, and pressure profiles in the supersonic burner experiments of the proposed Phase II program. Using a pulsed-dye laser rather than the ring-dye laser, NO fluorescence lineshapes in the jet will be recorded simultaneously with static cell absorption lineshapes to determine the local gas velocity. Mean temperature measurements will be made by scanning the laser beam across several isolated fluorescence features and comparing the measured intensity distribution to the Boltzmann population levels at a given temperature. The measured temperature profile will be used to fit the lineshape to a Voigt profile so as to extract the local gas pressure. These baseline profiles will be used to determine the instantaneous velocity imaging measurement accuracy over a range of velocity, temperature, and pressure conditions.

In summary, the results described above verify the feasibility of our Phase II approach by demonstrating that our understanding of the NO lineshape is sufficiently detailed that velocity-shifts may be measured in the presence of pressure and thermal broadening.